LAWRENCE
LIVERMORE
NATIONAL
LABORATORY

LLNL-JRNL-809380

Cosmogenic Radionuclide Production

P. N. Peplowski, J. T. Wilson, M. T. Burks, A. W. Beck, I. Jun, D. J. Lawrence, Z. W. Yokley

April 30, 2020

Nuclear Instruments and Methods in Physics Research B

Disclaimer

This document was prepared as an account of work sponsored by an agency of the United States government. Neither the United States government nor Lawrence Livermore National Security, LLC, nor any of their employees makes any warranty, expressed or implied, or assumes any legal liability or responsibility for the accuracy, completeness, or usefulness of any information, apparatus, product, or process disclosed, or represents that its use would not infringe privately owned rights. Reference herein to any specific commercial product, process, or service by trade name, trademark, manufacturer, or otherwise does not necessarily constitute or imply its endorsement, recommendation, or favoring by the United States government or Lawrence Livermore National Security, LLC. The views and opinions of authors expressed herein do not necessarily state or reflect those of the United States government or Lawrence Livermore National Security, LLC, and shall not be used for advertising or product endorsement purposes.

Nuclear Inst. and Methods in Physics Research B 446 (2019) 43–57

Contents lists available at ScienceDirect

Nuclear Inst. and Methods in Physics Research B

journal homepage: www.elsevier.com/locate/nimb

Cosmogenic radionuclide production modeling with Geant4: Experimental benchmarking and application to nuclear spectroscopy of asteroid (16) Psyche

Patrick N. Peplowski[a,*], Jack T. Wilson[a], Morgan Burks[b], Andrew W. Beck[a], Insoo Jun[c], David J. Lawrence[a], Zachary W. Yokley[a]

[a] Johns Hopkins Applied Physics Laboratory, 11100 Johns Hopkins Road, Laurel, MD 20723, USA
[b] Lawrence Livermore National Laboratory, 7000 East Avenue, Livermore, CA 94550, USA
[c] Jet Propulsion Laboratory, California Institute of Technology, 4800 Oak Grove Drive, Pasadena, CA 91109, USA

ARTICLE INFO

Keywords:
Gamma-ray spectroscopy
Geant4
Cosmogenic radionuclides
Activation
Asteroid
Planetary gamma-ray spectroscopy

ABSTRACT

Measurements of gamma-ray emissions from the decay of cosmogenic radionuclides provide an opportunity to characterize the elemental composition of a terrestrial planet or asteroid surface. We report on the development of a Geant4 application which models cosmogenic radionuclide production on metal-rich surfaces. The model was benchmarked using measurements of radionuclides produced during 1 GeV proton irradiation of a target made from the Campo del Cielo iron meteorite. The gamma-ray emitting radionuclides ^{58}Co, ^{57}Co, ^{56}Co, ^{54}Mn, ^{52}Mn, ^{51}Cr, ^{48}V, ^{46}Sc and ^{22}Na were observed following the irradiation. Our model reproduced the measured radionuclide production rates to within a factor of 2.5 or better. All but two of the elements (^{54}Mn, ^{46}Sc) have a perfect model-to-data match within their measurement uncertainties. The benchmarked model was used to predict cosmogenic radionuclide production on a large (~100-km radius) metal-rich asteroid. The results are relevant for planned gamma-ray measurements of the metallic asteroid (16) Psyche, which will be visited by the Psyche spacecraft in 2026. We found that galactic-proton-induced radionuclide decay is unlikely to be observed by the Psyche Gamma-Ray Spectrometer (GRS), however an intense solar proton event ($> 2 \times 10^6$ protons cm^{-2} over < 5 days) will produce measurable quantities of radioisotopes. Measurements of these radioisotopes could provide an independent method of determining the Ni-to-Fe ratio of materials at Psyche's surface. Such an analysis will require the use of radionuclide production cross sections to convert GRS-measured cosmogenic radionuclide decay rates to elemental composition information with the ~10% precision required for planetary geochemical studies.

1. Introduction

The surfaces of airless planetary objects (planets, moons, and asteroids) are subjected to constant bombardment by solar- and galactic-originating cosmic particles. Much of this cosmic radiation has sufficient kinetic energy to catastrophically disrupt incident atomic nuclei, dissociating the nuclei in a process called nuclear spallation. The number and type of residual (cosmogenic) nuclei produced via spallation depends on both the cosmic radiation environment and the elemental composition of the surface (e.g. [1,2]). With knowledge of the cosmic-ray environment and the relevant spallation cross sections, surface composition information can, in principle, be determined via measurements of cosmogenic radionuclide decay.

Spallation reactions produce residual nuclides in quantities that are inversely proportional to the difference between the mass of the initial (target) nuclide and the product (residual) nuclide (e.g., [3,4]). Spallation of the elements Fe and Ni typically results in production of the slightly-lower-mass elements Co, Mn, Cr, and V, which have a variety of radioactive isotopes. In contrast, the number of lower-mass radionuclides available from spallation of silicates (e.g. O, Mg, Si, Al) is limited. Thus, the number and concentration of cosmogenic radionuclides produced within iron meteorites is higher than in silicate-rich meteorites [5].

Measurements of cosmogenic nuclide concentrations have become a common tool for characterizing meteoritic materials. For example, the duration of exposure to cosmic radiation, as well as elapsed time since

* Corresponding author.
E-mail address: Patrick.Peplowski@jhuapl.edu (P.N. Peplowski).

https://doi.org/10.1016/j.nimb.2019.03.023
Received 12 October 2018; Received in revised form 5 February 2019; Accepted 13 March 2019
0168-583X/ © 2019 The Authors. Published by Elsevier B.V. This is an open access article under the CC BY-NC-ND license (http://creativecommons.org/licenses/BY-NC-ND/4.0/).

the end of exposure, is frequently characterized for meteorites via laboratory measurements of cosmogenic radionuclide abundances. There is extensive literature devoted to both modeling [1,2,6,7] and measuring (e.g., [8–10]) cosmogenic radionuclide concentrations in meteorites and lunar samples.

In-situ measurements of cosmogenic nuclide concentrations on planetary surfaces are more challenging than laboratory-based studies of meteorites. Orbital gamma-ray measurements may be sensitive to the presence of cosmogenic radionuclides, if the decay process includes gamma-ray emission. A metal-rich object like the asteroid (16) Psyche – hereafter referred to as Psyche – provides a unique opportunity to observe in situ cosmogenic radionuclide production and decay for a variety of isotopes that are less likely to be produced on rock- and ice-dominated worlds.

Asteroid Psyche will be surveyed from orbit by the Psyche spacecraft in 2026–2027 [11]. The Psyche spacecraft carries a Gamma-Ray and Neutron Spectrometer (GRNS; [12]) to characterize elemental composition from orbit. GRNS will use measurements of prompt gamma-ray emissions, resulting from neutron inelastic scattering and neutron radiative capture, to determine Psyche's near-surface elemental composition. Gamma-ray emissions from radionuclide decay, including cosmogenic radionuclides, will also be present. To date, the magnitude of gamma-ray emissions from the decay of cosmogenic radionuclides on Psyche has not been estimated, and therefore the likelihood of their detection by the Psyche GRNS investigation is unknown.

Radionuclide production in the cosmic-ray environment is a complex, multi-step process that involves a variety of nuclear processes that occur over many decades in energy (~10 MeV to > 100 GeV). A common approach to producing quantitative estimates of radionuclide production in this environment is to use radiation transport models. We adopted the Geant4 simulation toolkit for this task. Given the complexity of the simulations, an appropriate benchmark of the simulation outputs was deemed necessary to build confidence in our models. Our benchmark was a proton irradiation experiment of analog materials (an iron meteorite and a typical silicate rock; Section 3) at relevant proton energies (1 GeV; Section 2). The cosmogenic radionuclide concentrations produced during this experiment, determined via gamma-ray spectroscopy of the activated samples following irradiation (Section 4), provided the benchmark from which the Geant4 simulations were evaluated prior to carrying out full simulations for Psyche (Section 5). Model-based estimates of cosmogenic radionuclide production and decay in the galactic and solar proton environments were evaluated in the context of the Psyche GRNS measurement capabilities (Section 6). An example chemical result that could be obtained from Psyche GRNS measurements of cosmogenic radionuclides is presented.

2. Cosmogenic radionuclide production

2.1. Galactic cosmic-ray protons

The surfaces of airless solar system bodies are subjected to constant bombardment by galactic- and solar-originating cosmic particles. Galactic cosmic rays consist of protons (~90–95% by number), alpha particles (~5–10%), heavy (Z > 2) ions (< 1%), and electrons (< 1%), having energies up to > 100 GeV per nucleon (Fig. 1A; e.g., [13]). This study focuses exclusively on protons, although we note that alpha particles contribute to cosmogenic radionuclide production. A common method to account for alpha-particle-induced radionuclide production is multiplying proton-induced production rates by a scale factor (e.g., 1.55; [2]) and weighting by alpha particle fraction.

Many cosmic rays have energies far exceeding the binding energy of protons and neutrons in the nucleus (~1 to 10 MeV/nucleon), thus even a peripheral impact between a cosmic particle and a nucleus can impart sufficient energy to the nucleus to liberate nucleons and leave the target nucleon in a lower-mass (residual) state. As the probability for nucleon emission is a function of cosmic-ray energy, the type and number of residual nuclides produced during nuclear spallation depends on the spectral shape and flux of the cosmic rays.

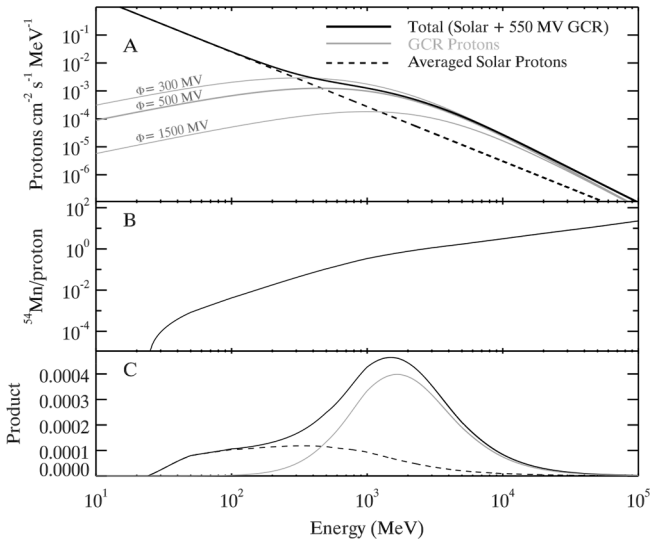

Fig. 1. (A) Solar- and galactic-cosmic-ray proton environment for Psyche. The solar component was derived from the formalism of Feynman et al. [18], and represents the likely proton environment during Psyche orbital operations at asteroid (16) Psyche. This spectrum is a cumulation of individual solar proton events (SPEs), divided by orbital mission duration, to produce a time-averaged spectrum. The galactic cosmic-ray (GCR) proton environment was calculated using Eq. (1) for three solar modulation parameters that bracket the likely values during the Psyche mission. (B) ^{54}Mn production, per incident proton, in a model Psyche (Table A1) as a function of proton energy. (C) The product of the data shown in Panels (A) and (B), highlighting the relevant energy ranges for radionuclide production by SPE (dashed line), GCR (grey line), and the total proton (black line) environments.

The galactic cosmic-ray (GCR) proton energy spectrum can be calculated using the GCR force-field approximation introduced by Castagnoli and Lal [14], who derived an analytic formula for calculating the 4π differential GCR proton spectrum G_p as a function of solar modulation parameter ϕ and particle kinetic energy T. This formalism was generalized by Lal [15] for use for any GCR particle ($G(\phi,T)$) as:

$$G(T,\phi) = A\frac{T(T+2E_0)\left(T+m+\phi\frac{Z}{A}\right)^{-\gamma}}{(T+\phi\frac{Z}{A})(T+2E_0+\phi\frac{Z}{A})} \quad (1)$$

where T is the kinetic energy of the GCR particle (in MeV), E_0 is the rest mass of the particle (in MeV; 938.3 MeV for protons and 3737.4 MeV for α), m is parameterized as ae^{-bT}, Z and A are the proton and nucleon numbers of the GCR particle. A, a, b, and γ values for protons and alpha particles were provided by Lal, [15] and were reproduced in Table 2 of McKinney et al. [16]. $G(\phi,T)$ has units of particles cm^{-2} s^{-1} MeV^{-1}. All GCR species (e.g. alpha particles) have similar spectral shapes when plotted in units of MeV/A.

Fig. 1A plots $G_p(\phi,T)$ for solar modulation values of 300, 550, and 1500 MV. These values represent typical minimum, average, and maximum solar modulation values occurring during the 11-year-long solar cycle (e.g. [17]). Thus, the GCR proton flux shown in Fig. 1A is expected to bound that at Psyche during the orbital mission. In contrast to the solar proton events, the GCR flux generally varies slowly and continuously as a function of time, with fluxes typically changing at the < 10% level on a day-to-day basis.

2.2. Solar cosmic-ray protons

Fig. 1A also details a differential energy spectrum for solar-originating cosmic-ray protons. The spectrum is the predicted cumulative fluence during Psyche's orbital mission phase (2026–2027), divided by

the duration of that mission phase. It was calculated following the methodology of Feynman et al. [18] and references therein. The spectrum is based on a statistical model and represents the most likely environment at Psyche during 2026–2027 as inferred from historical data. The figure depicts these solar protons as a time-averaged, steady-state fluence. In reality, these protons arrive at Psyche during distinct, randomly timed events of varying intensity, typically lasting hours to days. Thus, the actual solar proton environment at Psyche during GRNS measurements may differ from that shown in the plot, and the environment at any given moment does not correspond to that shown in Fig. 1A.

2.3. Cosmogenic radionuclide production

Cosmogenic nuclide production rates increase with increasing cosmic-ray energy, as higher-energy particles are more likely to induce spallation during the intranuclear cascade initiated by an impact between a cosmic-ray particle and a nucleus. In thick targets like planetary surfaces, the secondary particles liberated during the initial intranuclear cascade can be energetic enough to initiate further spallation reactions on other nuclei, known as internuclear cascades. In this thick-target regime, cosmogenic radionuclide production initially increases with depth, peaking at a depth of tens of cm beneath the surface [2,19].

The average number of secondary particles liberated via spallation increases with the energy of the primary particle, and so does the number of intranuclear cascades. Fig. 1B reports predictions from a radiation transport model (Section 5) that was used to estimate the rate of ^{54}Mn production (per GCR proton) as a function of incident proton energy in a large object like Psyche. ^{54}Mn is a common cosmogenic radionuclide produced primarily from spallation of ^{56}Fe via the reaction ^{56}Fe(p,2pn)^{54}Mn. Mn-54 has a half-life of 312 days, and its decay is usually (99.98%) accompanied by the emission of a characteristic gamma ray at 834 keV. It is this gamma ray that can be detected from orbit to yield information about the ^{54}Mn content of Psyche's surface.

The product of the proton flux (Fig. 1A) and radionuclide production probability (Fig. 1B) reveals the energy range over which the majority of cosmogenic radionuclide production occurs. For the full (galactic + solar) environment, the energy window of interest peaks at 1.5 GeV (Fig. 1c) The galactic-component-only environment peaks at slightly higher energy (~1.6 GeV), whereas the solar component contributes over a broad energy range extending from about 40 MeV to 1 GeV. Our sample irradiation benchmarking experiment (Section 4) was conducted at single proton energy of 1 GeV, close to the peak in the production times proton spectrum (1.5 GeV; Fig. 1C).

3. Samples

Our primary irradiation target was a 10 × 10 cm^2 area, 1.5-cm-thick, 1265-g slab of the iron meteorite Campo del Cielo (Fig. A1). Iron meteorites are thought to be fragments of disrupted planetary cores, with their in-space counterparts being the M-class asteroids, a taxonomy group that includes Psyche. Thus, Campo del Cielo is a candidate analog material for Psyche, and its elemental composition may be relevant to Psyche GRNS measurements. The elemental composition of the slab of Camp del Cielo used in this study (Table A1) was derived from measurements of other pieces of the Campo del Cielo meteorite [20,21].

Our irradiation experiment also included a second target, a small (256 g, 52.8 ± 3.4 cm^2) slab of bronzitite pyroxenite (BP). BP is composed of pyroxenes, a common silicate mineral on rocky solar system objects and the same mineral thought to be present on Psyche's surface at < 10% concentrations (6 ± 1%; [22]). The thickness of the BP slab was 1.5 cm, identical to the iron meteorite target, however its area was ~53% that of the iron meteorite slab (Fig. A1). The uncertainty in the area is a result of non-uniformity in the BP target thickness near the edges. Table A2 lists the elemental composition of the BP sample, as derived from a PIXE-induced x-ray fluorescence investigation of multiple spots on a portion of the BP sample that was removed prior to creating the BP irradiation target.

Prior to irradiation, measurements of gamma-ray emissions from both samples revealed no intrinsic radioactivity above background levels. Any residual cosmogenic radionuclides in the Campo del Cielo sample resulting from its exposure to the space radiation environment were below levels detectable via our laboratory gamma-ray measurements. All gamma-ray emissions observed following the irradiation experiment (Section 4) were therefore attributed to activation of the samples during the proton irradiation.

4. Experiment

4.1. Meteorite irradiation

Our samples were irradiated at the NASA Space Radiation Laboratory (NSRL; [23]), located at the Brookhaven National Laboratory (BNL). The proton beam was provided by two 15 MV Tandem Van de Graaff accelerators, and further accelerated to our desired energy of 1 GeV in the BNL Alternating Gradient Synchrotron booster. Beam bunches, which had a width of 300–400 ms, were pulled from the booster every 3.5 s and directed toward the NSRL beamline, where a series of quadrupole magnets shaped the beam to a 15 cm × 15 cm square which uniformly irradiated the samples [24]. The shaped beam bunches entered the open-air NSRL target room, where they traveled ~6 m to the target table. The samples were positioned on the target table, one at a time, on low-density polyethene foam blocks that were sized to keep the samples, but not the target table, in the path of the proton beam. This ensured that only primary, full-energy protons irradiated the samples. The samples were also encased in the polyethene foam to keep them in a fixed, upright position in the beamline. The foam was chosen as the target holder due to its low density and low nuclear charge (Z), which ensured minimal attenuation and down-scattering of the protons.

A proton fluence of 8×10^9 cm^{-2} was incident on each sample. Upstream ion chambers (ICs) counted proton events throughout each irradiation run. Once the target fluence was reached, the irradiation run was automatically terminated. Prior to irradiation, the IC was calibrated against a NIST-traceable thimble ion chamber, and a detailed analysis has shown that the overall dose uncertainty of the NSRL system is 3.6% [25].

The downstream digital beam imager (DBI) used a CCD camera to capture images of proton-induced fluorescence from a ZnS foil located in the beamline, downstream from the target. Fig. A1 shows example images of both targets acquired by the DBI. Horizontal and vertical profiles of the beam were derived from the CCD images acquired approximately once per minute. The images were used to confirm, and as necessary adjust, the beam profile in real time. This technique routinely achieves uniform irradiation, with < 3% variance across the sample, for all particle species and energies [25].

4.2. Activity measurements

4.2.1. On-site measurements

Following irradiation, the samples were transferred to an on-site target counting room at NSRL, where a high-purity germanium (HPGe) detector was used to measure gamma-ray emissions from the sample. For the Fe meteorite, we made the following on-site measurements:

1. 5 min live time, sample-to-detector distance of 53 cm, started ~16 min after irradiation;
2. 5 min live time, sample-to-detector distance of 53 cm, started ~20 min after irradiation;

Table 1
Radionuclides tentatively identified, but not quantified, during on-site gamma-decay measurements of the iron meteorite (composition listed in Table A1), as measured within 24 hrs of the proton irradiation. Nucleus identification is based on gamma-ray energy measurements only.

Nucleus	Decay	Half-life	Energy (keV)	Predicted by Geant4 Model?
^{67}Ge	ε	18.9 m	167.0, 511.0	No*
^{57}Ni	β^+	35.60 h	127.2, 511.0, 1377.6, 1757.6, 1919.5	Yes
^{61}Co	β^-	1.649 h	67.4	Yes
^{58}Co	ε	70.86 d	511.0, 810.8	Yes
^{56}Co	ε	77.236 d	511.0, 846.8, 1037.8, 1238.3	Yes
^{55}Co	ε	17.53 h	477.2, 511.0, 931.1, 1316.6, 1370.0, 1408.5	Yes
^{53}Fe	ε	8.51 m	377.9, 511.0	Yes
^{56}Mn	β^-	2.58 h	846.8, 1810.7, 2113.1, 2523.1, 2657.6, 2959.9, 3369.8	Yes
^{54}Mn	ε	312.20 d	834.8	Yes
^{52}Mn	IT	21.1 m	377.7	Yes
^{52}Mn	ε	5.591 d	511.0, 744.2, 848.2, 935.5, 1246.3, 1333.6, 1434.1	Yes
^{51}Cr	ε	27.7 d	320.1	Yes
^{49}Cr	β^+	42.3 m	62.3, 90.6, 152.9, 511.0	Yes
^{48}Cr	ε	21.56 h	112.3, 308.2, 511.0	Yes
^{48}V	ε	15.97 d	511.0, 944.1, 983.5, 1312.1, 2240.4	Yes
^{44}Ti	ε	59.1 y	67.9, 78.3	Yes
^{48}Sc	β^-	43.67 h	983.5, 1037.5, 1312.1	Yes
^{47}Sc	β^-	3.3492 d	154.4, 158.8, 159.3	Yes
^{46}Sc	β^-	83.79 d	889.3, 1120.5	Yes
^{44}Sc	IT	58.61 h	271.2	Yes
^{44}Sc	ε	3.97 h	511.0, 1157.0, 1499.5, 2656.5	Yes
^{43}Sc	ε	3.891 h	372.9, 511.0	Yes
^{44}K	β^-	22.13 m	1157.0, 1499.5, 2150.8, 2519.0	Yes
^{43}K	β^-	22.3 h	372.8, 396.9, 593.4, 617.5	Yes
^{42}K	β^-	12.355 h	1524.6	Yes
^{38}K	ε	7.636 m	511.0, 2167.5	Yes
^{41}Ar	β^-	109.6 m	1293.6	Yes
^{39}Cl	β^-	55.6 m	250.3, 985.9, 1091.1, 1267.2, 1517.5	Yes
^{38}Cl	β^-	37.23 m	1642.4, 2167.5	Yes
^{34}Cl[146.4]	IT	31.99 m	146.4	No
^{34}Cl[146.4]	ε	31.99 m	511.0, 1176.6, 2127.5, 3304.0	No
^{38}S	β^-	170.3 m	1941.9	Yes
^{37}S	β^-	5.05 m	3103.4	Yes
^{29}Al	β^-	6.56 m	1152.6, 1273.4, 2028.1, 2425.7	Yes
^{28}Al*	β^-	2.245 m	1779.0	Yes
^{28}Mg*	β^-	20.915 h	400.6, 941.7, 1342.2	Yes
^{27}Mg	β^-	9.458 m	843.7, 1014.5	Yes
^{24}Na	β^-	14.997 h	1368.6, 2754.0	Yes
^{7}Be	ε	53.22 d	477.6	Yes

* Geant4 model with “Shielding” physics list (see Appendix B). “Yes” indicates that the model predicted production of least 1000 nuclei during irradiation.

3. 103 min live time, sample-to-detector distance of 25 cm, started ~68 min after irradiation;
4. ~15 h live time, sample-to-detector distance of 25 cm, started ~305 min after irradiation.

The meteorite-to-detector distance was varied by necessity, as immediately following irradiation the activity of the meteorite was such that placing it too close to the detector resulted in unacceptably high dead time. For the silicate rock, we made the following measurements:

1. 5 min live time run, sample-to-detector distance of 56 cm,
2. 5 min live time run, sample-to-detector distance of 56 cm,
3. 5 min live time run, sample-to-detector distance of 56 cm, and
4. 10 min live time run, sample-to-detector distance of 15.3 cm.

Again, the distance was varied as needed to limit the detector dead time during each measurement.

The initial measurements were short (5 min) in order to facilitate identification of short-lived (e.g., half life $t_{1/2} \leq 1$ min) radionuclides. The longer measurements, taken hours after irradiation, were made with the goal of identifying longer-lived (~hr half-life) radionuclides in the samples. Tentative radionuclide assignments, made primarily on the basis of gamma-ray energy, are detailed in Tables 1 and 2. The majority of these assignments correspond to radioisotopes whose production was predicted by Geant4 radiation transport modeling of the irradiation experiment (Section 5.1). Quantitative radionuclide production measurements were not made using NSRL data, due to the varying target distances and resulting complications to deriving an instrument response model.

4.2.2. Long-term measurements

Following the target irradiation and NSRL on-site activity measurements, the samples were returned to the Planetary Nuclear Spectroscopy Laboratory at the Johns Hopkins Applied Physics Laboratory (APL) for long-term monitoring of radionuclide decay rates. The silicate rock was returned within a few days. The Fe meteorite required a decay period of approximately three weeks prior to being returned to APL. Upon arrival, gamma-ray emissions from the samples were repeatedly characterized with a 7.4-cm-diameter by 6.8-cm-long (73.5% relative efficiency) HPGe detector. The energy-dependent intrinsic gamma-ray photopeak detection efficiency (ε) and measurement solid angle (Ω) for this measurement geometry, and their systematic uncertainties, were derived from Geant4 modeling of the gamma-ray counting station (Appendix A).

The measurement plan included the following routine:

1. Energy calibration (^{137}Cs, ^{60}Co, ^{228}Th, and ^{55}Mn sources),
2. Fe meteorite measurement,
3. Room background measurement,
4. Silicate sample measurement,

Measurements 2–4 were typically each ~24 h long. The measurement

Table 2
Radionuclides tentatively identified, but not quantified, during on-site gamma-decay measurements of the silicate target (composition listed in Table A2), as measured within several hours of the proton irradiation. Nucleus identification is based on gamma-ray energy measurements only.

Nucleus	Decay	Half-life	Energy (keV)	Predicted by Geant4 Model?*
^{53}Fe	ε	8.51 m	377.9, 511.0	Yes
^{56}Mn	β^-	2.58 h	846.8, 1810.7, 2113.1	Yes
^{52}Mn[377.7]	IT	21.1 m	377.7	Yes
^{52}Mn[377.7]	ε	21.1 m	511.0, 1434.1	Yes
^{49}Cr	β^+	42.3 m	90.6, 152.9, 511.0	Yes
^{48}V	ε	15.97 d	511.0, 983.5, 1312.1	Yes
^{44}Ti	ε	59.1 y	67.9, 78.3	Yes
^{44}Sc	ε	3.97 h	511.0, 1157.0	Yes
^{43}Sc	ε	3.891 h	372.9, 511.0	Yes
^{42}K	β^-	12.355 h	1524.6	Yes
^{38}K	ε	7.636 m	511.0, 2167.5	Yes
^{41}Ar	β^-	109.6 m	1293.6	Yes
^{39}Cl	β^-	55.6 m	1267.2, 1517.5	Yes
^{38}Cl	β^-	37.23 m	1642.4, 2167.5	No
^{34}Cl[146.4]	IT	31.99 m	146.4	No
^{34}Cl[146.4]	ε	31.99 m	511.0, 1176.6, 2127.5, 3304.0	No
^{29}Al	β^-	6.56 m	1273.4, 2028.1, 2425.7	Yes
^{28}Al	β^-	2.245 m	1779.0	Yes
^{27}Mg	β^-	9.458 m	843.7, 1014.5	Yes
^{24}Na	β^-	14.997 h	1368.6, 2754.0	Yes

* Geant4 model with "Shielding" physics list (see Appendix B). "Yes" indicates that the model predicted production of least 1000 nuclei during irradiation.

routine was repeated periodically over the course of 8 months in order to fully characterize the decay curves of the radionuclides produced during irradiation.

4.3. Spectral analysis

The alternating room background and sample measurements were paired for the analysis of the measurements made at APL (Fig. 2, top panel). A background-subtracted spectrum (BGS) was created for each pair of measurements by subtracting the room background spectrum from the sample measurement (Fig. 2, bottom panel). The background spectrum was normalized in time to that of the sample measurement prior to subtraction. Per-channel statistical uncertainties for the BGS were derived from the original Poisson statistics of the two measurements. All gamma-ray features in the BGS were attributed to gamma-ray emissions from the sample. Known room background lines, for instance the 1460.8- and 2614.6-keV gamma-ray emissions from radioactive decay of ^{40}K and ^{232}Th decay daughters, respectively, were absent from the BGS.

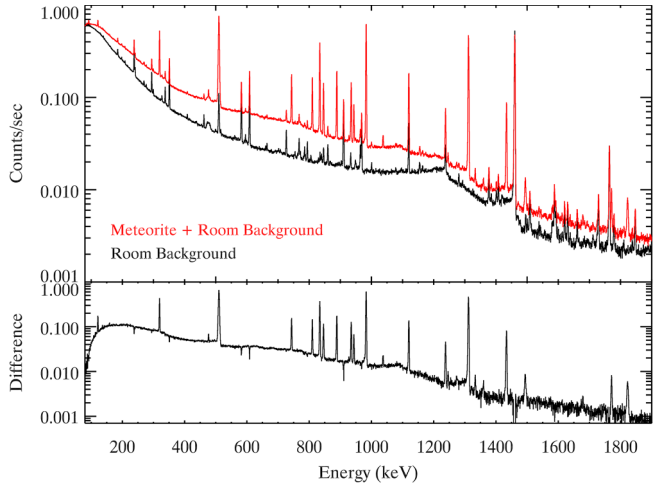

Fig. 2. Sample gamma-ray spectra from the iron meteorite target, acquired three weeks following the proton irradiation experiment. The top panel shows the measurements with (red) and without (black) the sample in place. The bottom panel shows the difference, which highlights gamma-ray peaks originating from the meteorite. Positive peaks, relative to the continuum, are signals above background and represent radioactive decay within the sample (Tables 1–4). Negative peaks, relative to the continuum, are room background artifacts of the spectral subtraction (difference) method. Peaks at 1494 and 1822 keV are pileup of ^{48}V decay lines (983 and 1311 keV) with the high-rate 511 keV annihilation line. (For interpretation of the references to color in this figure legend, the reader is referred to the web version of this article.)

A survey of the BGS spectra led to the identification of gamma-ray peaks of interest (POIs; Tables 3 and 4). Three characteristics were used for identification of their parent radioisotopes: the gamma-ray peak energies, the fact that the half-life must be of order days or longer to persist in the target weeks after irradiation, and the fact that any radioisotopes produced during irradiation must have $Z < 28$, as nickel is the highest-Z major component of the samples. This information was sufficient to identify the source isotope for each POI and determine its half life from existing nuclear data libraries.

For each POI, the number of events in the peak, in each measurement, was derived via regional peak summing of the respective BGS. Spectral fitting was not required, as none of our POIs overlapped with other spectral features. Three spectral windows were summed: one centered on the POI and sufficiently wide in energy to encompass the entire peak, and two centered on peak-free regions of the gamma-ray continuum at higher and lower energies than the POI. The two peak-free windows were half the width of the POI window. The number of events in the peak was derived as the sum of all events in the POI window, minus the sum of all events within the continuum windows. The peak count rate (C_γ) was derived by dividing this sum by the detector livetime during the sample run.

The measured gamma-ray peak count rate C_γ was derived for each POI (with energy E_γ) as a function of time. The individual C_γ values for each gamma-ray peak are compiled to produce a time series of measurements for each peak, denoted $C_\gamma(E_\gamma,t)$. $C_\gamma(E_\gamma,t)$ is used to derive the rate of decays in the sample, called the activity $A_\gamma(t)$, as

$$A_\gamma(t) = \frac{C_\gamma(E_\gamma, t)}{F_\gamma(E_\gamma) \in \Omega(E_\gamma)} \quad (2)$$

where F_γ is the fraction of decays that result in the emission of a gamma-ray with energy E_γ (Tables 3 and 4) and t is the time since irradiation. $\varepsilon\Omega(E_\gamma)$ and its systematic uncertainty (25%) were calculated

Table 3
Gamma-ray features and identification derived from long-term monitoring of gamma-ray emissions from the Fe meteorite target following proton irradiation.

Source Identification[b]				Measurements			
Isotope	Decay Energy (keV)	Gamma-Ray Fraction (F_γ)	Half-life (days)	Peak Maximum[a] (keV)	Fit half-life (days)	$\Delta t_{1/2}$ (σ)	Derived Activity @ Irradiation[c] A_0 (decays sec^{-1})
^{57}Co	122.1	0.856	271.7	121	129 ± 44	3.2	24.6 ± 5.5
^{51}Cr	320.1	0.0991	27.7	320.1	27.5 ± 1.6	1.3	1514 ± 191
^{7}Be	477.6	0.1044	53.22	477.2	41 ± 9	1.4	67 ± 16
Many	511.0	–	–	510.8	–	–	–
^{52}Mn	744.2	0.90	5.591	744.2	5.9 ± 0.7	0.5	1578 ± 299
^{58}Co	810.8	0.9945	70.86	810.4	65 ± 8	0.7	61.9 ± 3.6
^{54}Mn	834.8	0.9998	312.2	834.6	136 ± 25	7.2	132 ± 35
^{56}Co	846.7	0.9994	77.236	845.9	66 ± 8	1.4	48.5 ± 5.5
^{46}Sc	889.3	0.9986	83.79	889.0	67 ± 8	2.3	80 ± 14
^{52}Mn	935.5	0.945	5.591	935.2	5.3 ± 0.5	0.6	1471 ± 353
^{48}V	944.1	0.0787	15.97	942.8	15.8 ± 1.4	0.1	812 ± 60
^{48}V	983.5	0.9998	15.97	983.1	15.4 ± 0.6	1.0	883 ± 89
^{56}Co	1037.8	0.1450	77.236	1037.5	76 ± 41	0.0	40.3 ± 4.9
^{46}Sc	1120.5	0.9987	83.79	1120.0	67 ± 8	2.1	74 ± 12
^{56}Co	1238.3	0.6646	77.236	1238.3	65 ± 10	1.3	40.1 ± 4.7
^{48}V	1312.1	0.982	15.97	1311.7	15.6 ± 0.6	0.6	864 ± 51
^{52}Mn	1434.1	1.000	5.592	1433.4	6.0 ± 0.6	0.8	1525 ± 364
^{56}Co	1771.4	0.1541	77.236	1770.0	64 ± 13	1.0	41.0 ± 5.1

[a] Peak maximum location, not a fitted peak centroid.
[b] Values adopted from the compiled data in the National Nuclear Data Center (NNDC), nndc.bnl.gov.
[c] Derived activity at t = 0 (time of irradiation), A_0, using Eqs. (2) and (3). Errors include statistical uncertainties in the regional peak summing, systematic uncertainties in the irradiation (Section 4.1) and efficiency (Appendix A). Additionally, the uncertainty was adjusted (increased) when necessary to encompass A_0 values derived from fits with a fixed and free half life (Section 4.2.2).

Table 4
Gamma-ray features and identification derived from long-term monitoring of gamma-ray emissions from the silicate rock target following proton irradiation.

Source Identification[b]				Measurements			
Isotope	Decay Energy (keV)	Gamma-Ray Fraction F_γ	Half-life (days)	Peak Maximum[a] (keV)	Fit half-life (days)	$\Delta t_{1/2}$ (σ)	Derived Activity @ Irradiation[c] A_0 (decays sec^{-1})
^{51}Cr	320.1	0.0991	27.7	319.3	23.5 ± 12.5	0.3	25 ± 6
^{7}Be	477.6	0.1044	53.22	476.9	47.6 ± 7.0	0.8	96 ± 10
Many	511.0	–	–	510.8	–	–	–
^{54}Mn	834.8	0.9998	312.2	834.3	103 ± 36	5.8	2.0 ± 0.9
^{48}V	983.5	0.9998	15.97	983.0	16.8 ± 3.6	0.2	18 ± 2
^{22}Na	1274.5	0.9994	950.4	1273.8	203 ± 77.	9.7	3.5 ± 0.3

[a] Peak maximum location, not a fitted peak centroid.
[b] Values adopted from the compiled data in the National Nuclear Data Center (NNDC), nndc.bnl.gov.
[c] Derived activity at t = 0 (time of irradiation), A_0, using Eqs. (2) and (3). Errors include statistical uncertainties in the regional peak summing, systematic uncertainties in the irradiation (Section 4.1) and efficiency (Appendix A). Additionally, the uncertainty was adjusted (increased) when necessary to encompass A_0 values derived from fits with a fixed and free half life (Section 4.2.2).

from the Geant4 radiation transport model of our gamma-ray counting station (Appendix A). Fig. 3 shows an example of the output of application of Eq. (2) to our measured count rates, specifically the time series of the activity values for the 1771-keV gamma ray resulting from the decay of ^{56}Co.

We fit the measured activity rates with the standard radioactive decay formula as:

$$A(t) = A_0 e^{-\lambda t} \quad (3)$$

where λ is $\ln(2)/t_{1/2}$, and $t_{1/2}$ is the decay half life of the respective isotope. A_0 is the (unmeasured) activity of the sample immediately following the proton irradiation of the samples (at time $t = 0$).

Two fits were performed on the $A(t)$ data for each peak, using Eq. (3) and the IDL least-squares fitting routine MPFIT. In one fit, only A_0 was left as a free parameter, and $t_{1/2}$ was set to the known half life for the parent radionuclide of interest (Tables 3 and 4). The resulting A_0 value is denoted $A_0(1)$. A second fit to the same data was also performed, with both A_0 and $t_{1/2}$ left as free parameters. The results of that fit are denoted $A_0(2)$ and $t_{1/2}(2)$. In most cases, $t_{1/2}(2)$ is consistent (within errors) of the expected half life, and $A_0(1)$ and $A_0(2)$ are likewise consistent within their uncertainties. In that scenario, $A_0(1)$ and its error are recorded as the activity in Tables 3 and 4. But for some elements (see Tables 3 and 4), $t_{1/2}(2)$ is not consistent with the expected half life and $A_0(1)$ and $A_0(2)$ are likewise not consistent within their uncertainties. In that scenario, $A_0(1)$ is adopted as A_0 in Tables 3 and 4, but its uncertainties are inflated to encompass $A_0(2)$. We viewed adopting $A_0(1)$, but inflating its errors, as the most conservative approach to deriving accurate A_0 values. Examples of both fits are shown in Fig. 3 for the 1771.4-keV decay of ^{56}Co.

The agreement between the known and fitted half lives are generally good (Tables 3 and 4), however we note that the accuracy of our half-life measurements decreases as function the half life of the parent isotope increases. The three longest half-life isotopes studied here (^{57}Co, 271 days; ^{54}Mn, 312 days; ^{22}Na, 950 days) are the only isotopes for which the fitted and reference half lives differed by more than 3σ. While we found no conclusive explanation for this effect, we note that the longer the half life, the smaller the change in decay rate between any given measurement. Thus, longer half life measurements are more sensitive to systematic uncertainties in our experiment. Specifically, small changes in the sample-to-detector difference (e.g. Appendix A)

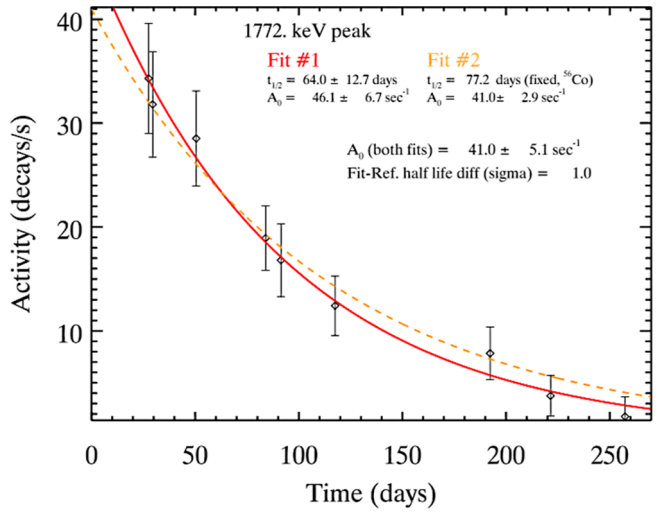

Fig. 3. Sample decay curve fit, for the 1771.4 keV peak from ^{56}Co decay, as measured in the Campo del Cielo iron meteorite. Time is days since sample irradiation. Two least-squared minimization fits of Eq. (3) to the data are shown in the plot. Fit 1, shown in red, has both half life ($t_{1/2}$) and initial activity (A_0) as free parameters. For Fit 2, shown as a dashed orange line, $t_{1/2}$ is fixed to the known value for ^{56}Co (77.2 days). The "A_0 (both fits)" value is A_0 derived from the fixed half life fit, but with an uncertainty that is inflated to encompass the free-parameter half life fit A_0 value. (For interpretation of the references to color in this figure legend, the reader is referred to the web version of this article.)

would have the biggest impact on long-lived isotopes, and the modeled magnitude of our systematic uncertainties (Appendix A) are sufficiently large to account for the deviations we observe in the half lives of these three elements.

The A_0 values for each gamma-ray peak (Tables 3 and 4) were converted to the number of parent nuclei (N_0) in the sample at the time of the irradiation as

$$N_o = \frac{A_0}{\lambda} \quad (4)$$

N_0 values for each POI are listed in Tables 3 and 4. Finally, we divided our N_0 values by the total proton fluence on target (8×10^9 cm^{-2}), times the target area (Section 3), to derive the number of atoms produced in the target per incident proton. These values, which appear in Table 5, provide the benchmark for our Geant4 model. In addition to the statistical uncertainties of the measurements, and the 25% uncertainty in our detector response, we added a 5% uncertainty to N_0 to account systematic uncertainties in the experiment (< 3% beam uniformity, < 3.6% beam fluence, see Section 4.1, added in quadrature).

5. Model spallation rates

5.1. Introduction

Our radionuclide production model was built using the Geant4 radiation transport toolkit [26–28], version 4.10.3. The model was based on the Hadr06 example, which has a built-in capability to track all particles and nuclei either excited by or formed during a spallation reaction. Note that residual nucleus production in the model is tracked regardless of whether the reaction-initiating particle was a primary proton (intranuclear cascade) or a secondary particle (internuclear cascade).

Modifications to the basis Geant4 code (example Hadr06) included replacing the custom Hadr06 physics list with G4PhysicsListFactory, which adds the flexibility to source any standard Geant4 physics list. We also replaced the G4ParticleGun class with G4GeneralParticleSource (GPS) class. GPS provides a more flexible

Table 5
Comparison of measured and modeled radionuclide production in the targets during the proton irradiation experiment.

Isotope	Energy (keV)	Measured N_0/proton[a]	Modeled Atoms/proton[b]	Meas./Model Ratio
Campo del Cielo Meteorite Target				
^{58}Co	810.8	$(6.6 \pm 1.0) \times 10^{-4}$	7.58×10^{-4}	0.9 ± 0.1
^{57}Co	122.1	$(1.0 \pm 0.3) \times 10^{-3}$	1.15×10^{-3}	0.9 ± 0.3
^{56}Co	846.7	$(5.7 \pm 1.2) \times 10^{-4}$	8.85×10^{-4}	0.6 ± 0.1
	1037.5	$(4.7 \pm 1.0) \times 10^{-4}$	"	0.5 ± 0.1
	1238.3	$(4.7 \pm 1.0) \times 10^{-4}$	"	0.5 ± 0.1
	1771.4	$(4.8 \pm 1.1) \times 10^{-4}$	"	0.5 ± 0.1
^{54}Mn	834.8	$(6.2 \pm 2.3) \times 10^{-3}$	4.64×10^{-3}	1.3 ± 0.5
^{52}Mn	744.2	$(1.3 \pm 0.4) \times 10^{-3}$	1.06×10^{-3}	1.3 ± 0.4
	935.5	$(1.2 \pm 0.4) \times 10^{-3}$	"	1.3 ± 0.4
	1434.1	$(1.3 \pm 0.4) \times 10^{-3}$	"	1.2 ± 0.4
^{51}Cr	320.1	$(6.3 \pm 1.4) \times 10^{-3}$	5.41×10^{-3}	1.2 ± 0.3
^{48}V	944.1	$(2.0 \pm 0.3) \times 10^{-3}$	2.24×10^{-3}	0.9 ± 0.2
	983.5	$(2.1 \pm 0.4) \times 10^{-3}$	"	1.0 ± 0.2
	1312.1	$(2.1 \pm 0.3) \times 10^{-3}$	"	0.9 ± 0.1
^{46}Sc	889.3	$(1.0 \pm 0.3) \times 10^{-3}$	4.20×10^{-4}	2.4 ± 0.6
	1120.5	$(9.4 \pm 2.4) \times 10^{-4}$	"	2.2 ± 0.6
Bronzite Pyroxenite Target				
^{54}Mn	834.8	$(1.8 \pm 1.1) \times 10^{-4}$	1.15×10^{-4}	1.6 ± 1.0
^{51}Cr	320.1	$(2.0 \pm 0.8) \times 10^{-4}$	1.52×10^{-4}	1.3 ± 0.5
^{48}V	983.5	$(8.4 \pm 2.3) \times 10^{-5}$	6.80×10^{-5}	1.2 ± 0.3
^{22}Na	1273.8	$(9.8 \pm 4.4) \times 10^{-4}$	8.00×10^{-4}	1.2 ± 0.6

[a] Number of atoms produced during irradiation, from A_0 (Tables 3 and 4) using Eq. (4).
[b] Total nuclide production per proton predicted by Geant4 model, using the Shielding physics list (see Section 5).

option for defining primary particle parameters, and facilitates including custom GCR and SPE energy spectra for the Psyche simulations (Section 6). The final change to the Hadr06 code was replacing the target geometry, and at this stage the code was bifurcated into two versions. The first version replicated the NSRL irradiation experiments detailed in Section 4.1. This geometry included the sample (size, elemental composition, density) and the foam holders, and for this version of the code GPS was used to define a plane wave of 1 GeV protons that uniformly illuminated the target. The second geometry is for asteroid Psyche, and is discussed in detail in Section 6.

A crucial parameter for Geant4 modeling is the selection of the physics list, which prescribes the transport and interaction processes for the primary protons through the target, secondary particle generation, and the primary- and secondary-particle-induced intranuclear and internuclear cascades that lead to the creation of residual nuclides, including radionuclides. Geant4 physics lists do not directly incorporate measured isotope production cross sections for hadronic interactions. Instead, at high energies the physics lists invoke intranuclear cascade models – e.g., Bertini (BERT), Binary Ion Cascade (BIC), and the Liege Intranuclear Cascade Model (INCL) – that provide the basis for predicting the final state of the incident nucleus. At lower energies, a compound nucleus is formed and decays stochastically into fragments. The characteristics of the residual nuclei are determined by a set of model parameters such as the density of states in the excited nucleus, the slope of the exponential that describes the outcome (mass) of a nucleus following nuclear evaporation, and the branching ratios for particle emission. These processes often leave the residual nuclei in excited states. De-excitation models use parameters derived from a large set of energy- and atomic-mass-dependent values to determine how nuclear de-excitation occurs, e.g. nuclear disintegration, fission, hadron emission or gamma emission [29].

Geant4 offers many standard physics lists that are appropriate for our application, including QGSP_BIC_HP, QGSP_BERT_HP, QGSP_INCLXX_HP, FTFP_BERT_HP, FTFP_INCLXX_HP, Shielding, ShieldingLEND, and QBBC [30]. BIC, BERT, and INCLXX were described in the prior paragraph. QGSP is the "Quark-Gluon String" (QGS)

with Pre-compound (P) nucleus model. FTFP is the Fritof with Pre-compound nuclear model. These physics lists have been validated for high-energy (> 100 MeV) hadronic reactions and include precision neutron cross section libraries via the Geant4 class NeutronHP (denoted via the "_HP" suffix on the physics list name). The Shielding physics list is based on FTFP_BERT_HP, but includes neutron cross sections derived from the Japanese Evaluated Nuclear Data Library (JENDL; [31]) and ion interactions from the Quantum Molecular Dynamics (QMD) model. Shielding is recommended for space physics and radiation shielding applications. The variant ShieldingLEND uses a different neutron interaction library, the low-energy nuclear database (LEND) library, developed by Lawrence Livermore National Laboratory as an alternative to the ENDF-based files used in the NeutronHP package. Finally, QBBC utilizes a combination of the BERT and BIC intranuclear cascade models and a neutron cross section model in lieu of the cross section libraries for faster computational time.

For all simulations, the following options were used to improve neutron-induced reaction accuracy and/or lower computational time for the models:

```
export G4NEUTRONHPDATA='path_to_Geant4_data'/ENDF-VIII.0
export G4NEUTRONHP_NEGLECT_DOPPLER = 1
export G4NEUTRONHP_DO_NOT_ADJUST_FINAL_STATE = 1
export G4NEUTRONHP_SKIP_MISSING_ISOTOPES = 1
export AllowForHeavyElements = 1
```

as recommended in the Geant4 Application Developers Guide [32]. Note that the neutron data is retrieved from the ENDF-VIII Evaluated Nuclear Data Files library, version 8 [33], which are generally valid for neutron energies from thermal (< 0.2 eV) up to 20 MeV.

The irradiation experiment described in Sections 3 and 4 was designed to provide a test of the accuracy of Geant4 physics lists to predict radionuclide production at our energies of interest. The Geant4 model of the BNL irradiation experiment was run with 8×10^7 protons on target for each physics list. For each run, the total number of residual nuclides produced was tallied and divided by 8×10^7 to determine the nuclide production per incident proton. This quantity was directly compared to the measured nuclide production per incident particle values (Table A3). Shielding provided the best match to the iron meteorite data (measurement to model ratio of 1.1), whereas QGSP_BIC_HP, QGSP_BERT_HP, and QBBC all provided the best matches to the silicate data (ratio of 0.9). Overall, the Shielding physics list provided the best match to the iron meteorite and silicate target data (ratio of 1.15; see Table A3), and it was adopted for all subsequent modeling.

Fig. 4 shows the element-by-element ratio of measured-to-modeled radionuclide production resulting from the Shielding physics list. A measured-to-modeled ratio of one denotes perfect agreement. For all isotopes we measured, the model reproduces the measurement to within a factor of 2.5 or better. For all but two isotopes, ^{56}Co and ^{46}Sc, the measured-to-modeled radionuclide production values are one (perfect agreement) within the statistical precision of our measurements.

In addition to those elements shown in Fig. 4, gamma-ray emissions from ^{7}Be were also observed in both targets following the irradiation experiment (Tables 3 and 4). ^{7}Be production is predicted by the model, however the measurement-to-model ratio was found to be exceptionally high, indicating that the model is underpredicting the amount of ^{7}Be produced within the target. Addition of the lightweight (H-, C-bearing) foam holders to the model improved the match, suggesting that our targets may have been contaminated by implanted ^{7}Be, produced via ^{12}C(p,p'^{7}Be)^{6}Li reaction in the foam holders. However, spallation models like INCL and Bertini regularly under predict the production of light clusters like ^{7}Be, as they are produced during both the cascade and evaporation stages of a spallation reaction. Production of clusters during the cascade stage is not well understood [34]. As a consequence, we do not attempt to interpret the ^{7}Be production resulting from our proton irradiation of the samples.

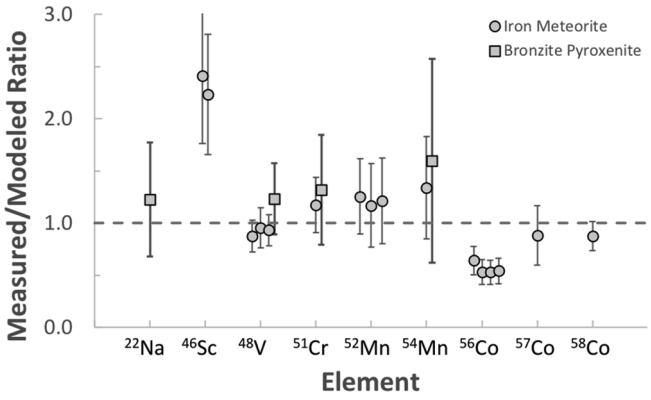

Fig. 4. Comparison of measured to modeled radionuclide production in the two samples. Elements are ordered by increasing atomic number. These values demonstrate factor of 2.5 or better agreement between the modeled and measured radionuclide production rates. The model was produced with Geant4 using the Shielding physics list (Appendix B).

6. Application to nuclear spectroscopy of asteroid (16) Psyche

6.1. Overview

Planetary nuclear spectroscopy uses gamma-ray emissions from a planet's surface, typically measured from orbit, to characterize the elemental composition of the surface. Here "planetary surface" denotes the uppermost ~1 m of materials on any object (planet, moon, asteroid) whose surface is exposed to the space radiation environment. Broadly, gamma-ray spectroscopy investigations involve:

1. Gamma-ray measurement acquisition and data quality filtering,
2. Spectral summing and gamma-ray peak fitting,
3. Corrections for systematic variability (e.g., altitude, cosmic ray flux),
4. Corrections for detector response (e.g., converting peak rate to peak flux), and finally,
5. Iterative comparison to radiation transport models to relate gamma-ray emissions to elemental composition.

To date, these studies have used gamma rays produced following neutron inelastic scattering and neutron radiative capture reactions, as well as from the decay of primordial radionuclides (^{40}K, ^{228}Th, ^{238}U). Numerous studies have validated the accuracy of planetary nuclear spectroscopy investigations, including the radiation transport modeling component, at a wide range of objects that includes the Moon [35], Mars [36], Mercury [37], asteroid 4 Vesta [38], and asteroid 433 Eros [39]. Similar efforts have validated the modeled fluxes of neutrons produced by cosmic rays [16,40–42], a critical parameter for the gamma-ray production process.

The methodology outlined above also provides a framework for using measurements of cosmogenic radionuclide decays to derive elemental composition information. What is lacking is a validation of the radiation transport models capability to accurately and quantitatively predict cosmogenic radionuclide production. The processes leading to radionuclide production are sufficiently different from the neutron-induced gamma-ray production processes that additional validation is warranted. Our meteorite irradiation experiment showed that, at least for long-lived, gamma-ray emitting isotopes of Co, Cr, Mn, V, Sc, and Na produced by 1 GeV irradiation of a thick target, the models are accurate within a factor of 2.5 (Fig. 4). Factor of 2.5 precision is inadequate for planetary nuclear spectroscopy studies, where ≤10% precision is required for geochemical studies. However, this precision is sufficient

for feasibility studies seeking to determine if cosmogenic radionuclide decay is observable from orbit.

The asteroid Psyche (mean radius = 113 km; [43]) will be the subject of a nuclear spectroscopy investigation in 2026, when the Psyche spacecraft arrives in orbit [11]. The Psyche project's prime mission includes a low-altitude (~80 km) orbit [44], from which the prime GRNS science measurements will be obtained [12]. The ability of GRNS to measure cosmogenic radionuclides from this orbit is examined here using the benchmarked Geant4 model.

In our Geant4 model, Psyche was treated as a 113-km-radius sphere made of material with an identical composition as the Campo del Cielo meteorite (Table A1). This composition is suggested by remote sensing evidence that Psyche has a high-density (e.g., [43,45]) and a metal-rich surface [43,46] mixed with ≤10% silicates [21,47]. Geant4 GPS (Section 5) was used to define an isotropic proton source that uniformly illuminates Psyche. Two proton energy distributions were examined. The first is the GCR proton spectrum, as defined in Eq. (1) and calculated for a solar modulation value of 550 MV (Fig. 1A). The results of this simulation are discussed in Section 6.2. The second proton energy distribution corresponds to a solar proton source with a power-law spectral shape as shown in Fig. 1A. The results of this simulation are presented in Section 6.3. For both galactic and solar protons, the simulations include particles with E > 30 MeV only, as lower-energy protons do not contribute to radionuclide production (e.g., Fig. 1B). Following completion of the simulations, the number of radionuclides produced within Psyche was divided by the number of modeled protons to yield the number of radionuclides produced per proton.

6.2. Galactic-proton-induced signals

Time-dependent concentrations of GCR-induced radionuclides in Psyche's near-surface materials were calculated using a secular equilibrium formalism that describes the balance between time-dependent radionuclide production and continuous radionuclide decay. The formalism for calculating the radionuclide concentration per unit area (N_a(t)) as a function of time is:

$$N_a(t) = N_a(t - \Delta t) + N_{GCR}(t)R_P - N_a(t - \Delta t)[1 - e^{(-\lambda \Delta t)}] + N_a(0) \quad (5)$$

where Δt is the time step of our numerical calculation (0.5 days, much smaller than the half lives of the elements considered in this study), N_{GCR}(t) is the GCR rate in units of protons $cm^{-2}s^{-1}$, and R_P is the modeled radionuclide production rate per incident GCR (Table 6). R_P values were modeled for each isotope of interest (Section 5) using the Geant4-modeled production rate per GCR proton (Section 6.1). Integrated GCR proton fluxes, N_{GCR}(t), historically range from approximately 1.5 to 5.5 cm^{-2} s^{-1} over the 11-year solar cycle. We incorporate this into our calculation via a sinusoidal function having a period of 11 years. This function mimics the historical behavior of GCRs, as measured at Earth, over the past ~100 years (e.g., [17,48–50]).

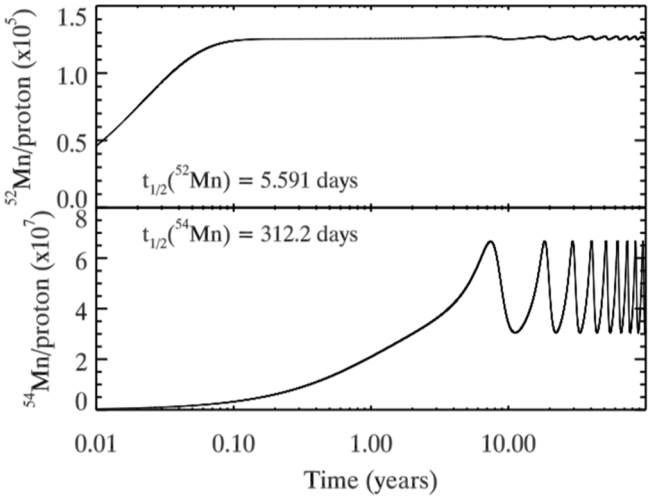

Fig. 5. GCR-induced radionuclide production per GCR, for ^{52}Mn (Top) and ^{54}Mn (bottom). The isotopes were chosen as their half lives span the range of interest of this study. The short-lived ^{52}Mn quickly (~0.1 yrs) reaches equilibrium with the GCR environment, whereas ^{54}Mn approaches equilibrium after ~3 yrs, after which point its concentration varies in proportion to the GCR variability, due to the fact that the GCR varies at a time scale that is shorter than the half life of ^{54}Mn.

Eq. (5) is used to track the concentration of each isotope for a total of 100 years, assuming an initial concentration (N_a(0)) of zero. Each radionuclide of interest reaches secular equilibrium with the source GCR flux within a few years (Fig. 5), thus the equilibrium value for each isotope is achieved within the 100-year time scale we explored. Fig. 5 shows the results of the calculation for ^{52}Mn and ^{54}Mn, where the equilibrium with the production rate is shown to be achieved at t ≈ 0.1 and 3 years, respectively.

The time dependent gamma ray emission rate at the surface was also calculated on a time-step basis. For each time step, the number of decays occurring in that time interval (e.g. Eq. (3)) was multiplied by the fraction of decays accompanied by emission of a gamma-ray of interest (F_γ values listed in Tables 3 and 4) and the probability that the gamma-ray will escape the surface unattenuated (Eqs. (1) and (2) of [51]). The probability that a gamma ray escapes the surface with its full energy depends on the amount of intervening material. We calculated surface escape probabilities using a Monte Carlo code that generates radionuclides with a depth profile matching prior calculations of Ammon et al. [19]. Specifically, we adopted the Ammon et al. depth profile for ^{53}Mn production in a large (10 m) iron meteoroid. That radionuclide production depth profile extended to depths of ~100 cm,

Table 6
Modeled rates for radionuclide gamma-ray emissions resulting from galactic cosmic-ray (GCR) protons.

Nuclide	Gamma-ray energy (keV)	Nuclei per GCR proton (R_P)	Min-to-Max equilibrium flux at surface ($cm^{-2}s^{-1}$)	Min-to-max rate in detector (s^{-1})[#]	Reference Continuum Rate ($s^{-1}keV^{-1}$)[▽]
^{58}Co	810	3.92×10^{-1}	$(0.7–2.7) \times 10^{-7}$	$(0.8–3.2) \times 10^{-7}$	1.5×10^{-2}
^{57}Co	121	2.59×10^{-1}	$(0.6–1.8) \times 10^{-8}$	$(2.3–6.9) \times 10^{-8}$	3.5×10^{-1}
^{56}Co	846	1.32×10^{-1}	$(2.7–9.7) \times 10^{-8}$	$(0.3–1.2) \times 10^{-7}$	1.4×10^{-2}
^{51}Cr	320	1.08×10^{0}	$(0.8–3.1) \times 10^{-8}$	$(2.3–9.0) \times 10^{-8}$	2.5×10^{-1}
^{54}Mn	834	1.81×10^{-1}	$(2.7–7.5) \times 10^{-7}$	$(3.2–9.0) \times 10^{-7}$	1.4×10^{-2}
^{52}Mn	1434	8.24×10^{-1}	$(0.5–1.9) \times 10^{-7}$	$(0.4–1.5) \times 10^{-7}$	1.1×10^{-2}
^{48}V	983	3.59×10^{-3}	$(0.4–1.4) \times 10^{-7}$	$(0.4–1.5) \times 10^{-7}$	1.4×10^{-2}
^{46}Sc	889	1.70×10^{-1}	$(0.8–2.8) \times 10^{-8}$	$(1.0–3.4) \times 10^{-8}$	1.4×10^{-2}

[#] Calculated from the min-to-max gamma-ray flux at the surface (e.g. Fig. 5), correcting for the spacecraft altitude above Psyche's surface (0.8 body radii), multiplied by the detector area (25 cm^2) and the GRS gamma-ray detection efficiency at the relevant gamma-ray energy, adopted from Peplowski et al. [57].

[▽] Measured gamma-ray continuum rate, from the MESSENGER Gamma-Ray Spectrometer, as observed at an altitude of 0.8 body radii from Mercury, the equivalent orbit to that planned for Psyche GRNS observations of Psyche.

peaking at ~5 cm.

Our calculated mean radionuclide gamma-ray emission rates, upon reaching equilibrium with the GCR environment, are listed in Table 6. The ^{54}Mn 834-keV gamma-ray emission rate, the highest we calculated, never exceeds 7.5×10^{-7} cm^{-2} s^{-1}. At 0.8 body radii altitude, this corresponds to a GRS-measured count rate of 9×10^{-7} s^{-1} (in a 25 cm^{-2} detector), an estimate that includes altitude effects (solid angle) and detection efficiency. The MESSENGER GRS, an identically sized, identical technology gamma-ray spectrometer, measured a gamma-ray continuum rate of 1.4×10^{-2} s^{-1} keV^{-1} at 834 keV at a Psyche-equivalent orbit of 0.8 body radii altitude above the surface of the planet Mercury. This background rate is many orders of magnitude higher than the GCR-induced rate. As the production and gamma-ray emission rates for ^{54}Mn are higher than all other radionuclides studied here, we conclude that GCR-induced radionuclide production and decay will be undetectable by the Psyche GRNS for the elements modeled.

6.3. Solar-proton-induced signals

In contrast to GCRs, solar protons are delivered to Psyche during short (~1 to 10 day long), high-fluence events (termed solar proton events, or SPEs) that occur with a frequency and intensity that varies with the 11-year-long solar cycle. In contrast with GCR-induced radionuclide production, SPEs offer a mechanism to rapidly produce large concentrations of cosmogenic radionuclides in a planetary surface.

This section details a formalism for calculating the > 30 MeV SPE proton fluence (Φ_p) needed to produce a measurable gamma-ray flux at Psyche's surface. The flux of gamma rays at Psyche's surface (ϕ_γ) is calculated from the decay rate at the surface as:

$$\phi_\gamma = A(t) F_\gamma \eta \quad (6)$$

where A(t) is the activity (decay rate) in the surface at time t, F_γ is the fraction of decays that are accompanied by emission of characteristic gamma rays (see Tables 3 and 4), and η is the probability that the gamma ray will escape the surface. η accounts for gamma-ray emission angle (e.g. was the gamma-ray directed toward space) and scattering in the surface. η was calculated from an analytical model that assumed isotropic gamma-ray emission in an Fe-Ni surface from random depths of up to 0.3 cm, the mean range of solar protons in Fe-Ni metal. Scattering probabilities were calculated for pure Fe-Ni metal, using Eqs. (1) and (2) of [51].

A(t) was calculated from the number of radionuclides produced during the SPE (N_0) as:

$$A(t) = \lambda N_0 e^{-\lambda t} \quad (7)$$

where t is the time since the end of the SPE. Half lives for our radionuclides of interest are listed in Tables 3 and 4. Note that our calculation assumes that the SPE duration was much shorter than the half life, such that the number of radionuclides at the end of the event is the same as the number of radionuclides produced during the event.

N_0 was related to the proton fluence Φ_p and Geant4-modeled radionuclide production rates (R_p) as:

$$N_0 = \Phi_p R_p \quad (8)$$

R_p values, listed in Table 7, were calculated from a Geant4 model (Section 5.1), using a surface-incident SPE flux whose spectral shape was identical to the solar proton spectrum shown in Fig. 1a, as detailed in Section 6.1. The solar proton spectrum of Fig. 1 is the time-averaged sum of all predicted events during the Psyche investigation. Thus, it is not necessarily representative of any single event that might occur, but its shape is representative of a broad range of events expected in the Psyche mission timeframe.

Eqs. (6)–(8) provided the basis for calculating the SPE fluences needed to produce measurable radionuclide decay on Psyche by solving for Φ_p as:

$$\Phi_p = \frac{\phi_\gamma}{R_p e^{-\lambda t} \lambda \eta F_\gamma} \quad (9)$$

For this calculation, we set ϕ_γ to be equal to the continuum rates listed in Table 6, and t = 10 days. The t value of 10 days was adopted to account for the fact that SPEs frequently result in a temporary suspension of GRS measurements [52]. Ten days was deemed sufficient time to resume nominal GRS data acquisition. Table 7 lists the > 30 MeV SPE fluences (Φ_p) needed to produce measurable (rate ≥ continuum) quantities of the radionuclides of interest to this study (Section 5). The values range from 1.9×10^6 protons cm^{-2} (for ^{52}Mn) to 8.8×10^9 protons cm^{-2} (for ^{22}Na).

To calculate the likelihood that events meeting the fluence requirements listed in Table 7 will occur at Psyche during the low-altitude observation campaign, we performed the following analysis to estimate the frequency and intensity of SPE events at 3 AU (Psyche's mean orbital distance). The approach we chose was to start with a database of SPE events at 1 AU, specifically an update of the solar proton event (SPE) database of Jun et al. [53]. This update catalogs all SPE events observed from July 1977 to November 2015. This process made the following two assumptions/simplifications:

Table 7
Solar proton event (SPE) fluences required to produce cosmogenic radionuclides with measurable gamma-ray emissions, 10-days after the SPE.

			Equivalent Event at 1 AU		
Nuclide	Radionuclides per proton (R_p)[▽]	(> 30 MeV) Proton Fluence (cm^{-2})[△]	Fluence (cm^{-2})[□]	Number of Events[#]	Event Frequency (yr^{-1})[*]
^{58}Co	3.3×10^{-3}	1.3×10^7	5.2×10^7	25	0.6
^{57}Co	2.4×10^{-3}	1.2×10^9	4.8×10^9	0	0
^{56}Co	1.5×10^{-3}	1.3×10^7	5.2×10^7	25	0.6
^{51}Cr	8.1×10^{-3}	2.0×10^8	8.0×10^8	5	0.1
^{54}Mn	9.7×10^{-3}	7.5×10^6	3.0×10^7	36	0.9
^{52}Mn	1.8×10^{-3}	1.9×10^6	7.6×10^6	64	1.6
^{48}V	1.7×10^{-3}	3.3×10^6	1.3×10^7	50	1.2
^{46}Sc	2.6×10^{-4}	7.8×10^7	3.1×10^8	11	0.3
^{22}Na	1.9×10^{-5}	8.8×10^9	3.5×10^{10}	0	0

□ Respective fluence at 1 AU, calculated by scaling as $R^{-2.5}$ power, as suggested by [54].
▽ From the Geant4 model, using a proton energy distribution identical to the solar proton data shown in Fig. 1.
△ Fluence required to produce a gamma-ray count rate equal to the gamma-ray continuum rate, derived from MESSENGER GRS data collected at an equivalent orbital altitude as planned for Psyche GRNS.
* Number of events divided by 41.1 years, the timespan of the SPE database, providing the frequency for the respective SPE averaged over ~4 solar cycles.
# Number of SPEs, observed at Earth, with > 27.2 MeV fluences exceeding the equivalent fluence at 1 AU. Database includes 41 years of observations, and is an update to Jun et al. [53].

1. We assumed the simplistic scenario wherein Psyche was directly "downstream" of Earth during each SPE in the database. The intensity at 3 AU is calculated from the value at 1 AU using a $r^{-2.5}$ radial dependence, following Feynman and Gabriel [54]. This ignores the strong solar-longitude dependence of SPE intensity, and Feynman and Gabriel [54] noted that variations ranging from r^{-2} to r^{-3} are expected. Lario et al. [55] observed a proton-energy dependence to the radial scaling, and reported scaling factors of $r^{-2.1}$ and $r^{-1.0}$ for 4–13 MeV and 27–37 MeV protons, respectively, however due to the wide range of energies relevant to our study (> 30 MeV) we adopted the more generalized $r^{-2.5}$ dependence.
2. We ignored the 11-year-period cycle of solar event activity, which influences the probability that a SPE will occur. Instead, the number of SPE events within the SPE catalog whose fluence was sufficient to produce a given radionuclide (Table 7) was divided by the total time span of the SPE database (1977 to 2015; 38 years) to provide a solar-cycle-averaged event frequency.

The results of this analysis are shown in Table 7. The estimated frequency of an SPE event with sufficient fluence to produce measurable quantities of a given element are: ^{58}Co and ^{56}Co, 0.6 SPE year^{-1}; ^{54}Mn, 0.9 SPE year^{-1}; ^{52}Mn, 1.6 SPE year^{-1}; ^{48}V, 1.2 SPE year^{-1}. The low-altitude orbit phase of the Psyche mission is planned to last for 100 days (0.27 years), meaning that a sufficiently large SPE as needed to produce measurable gamma decays from the radionuclides has a probability of ≤40% (for ^{52}Mn) or lower, depending on the radionuclide of interest.

6.4. Radionuclide science at Psyche

Although we concluded that GCR-induced activation is unlikely to be measured by the Psyche GRNS, there is a moderate probability that an SPE with sufficient fluence to measurably activate Psyche's surface will occur during the 100-day-long low-orbit phase of the Psyche mission. For the SPE-activation scenario, we modeled radionuclide production on Psyche (per incident proton) for a series of hypothetical compositions with varying Ni-to-Fe content. The results of this model showed that SPE-induced production of ^{58}Co, ^{57}Co, and ^{56}Co increases with increasing Ni content, whereas all other radionuclides decreased in production (per SPE proton) with increasing Ni content. The ratio of isotopic Co production to that of any other element therefore tracks with the Ni-to-Fe ratio, and such a measurement can therefore be used to derive the Ni-to-Fe ratio. Fig. 6 provides an example, showing the ratio of ^{58}Co to ^{52}Mn production following an SPE as a function of the Ni content of a model of Psyche with varying Ni content. Such a measurement would proceed as follows:

1. As SPE event illuminates Psyche with a high fluence of energetic protons (see Table 7 for fluence details).
2. Based on prior experience, such an event may force the Psyche spacecraft or Psyche GRNS to enter safe mode, interrupting measurements. Recovery and resumption of nominal GRS science operations can take ~10 days.
3. Upon resumption of measurements, radionuclide decay gamma rays are identified in the GRS spectra, and the N_0 values are derived (see Eqs. (2)–(4)).
4. The ratio of N_0 values can be compared to a model relationship (e.g. Fig. 6) to derive the Ni-to-Fe content of Psyche's surface.

The final step requires confidence in the radionuclide production rates derived from the model. This study revealed that Geant4 models of radionuclide production are accurate to within a factor of 2.5 for the isotopes considered here, and consistent with perfect agreement for all but two of the isotopes (Fig. 4). However, we note that measurements of the Ni-to-Fe content of Psyche's surface need to be made with < 10% precision for the Psyche GRNS investigation. Thus, if this technique is carried out using Psyche GRNS data, detailed radionuclide production cross sections (e.g. [56]) and calculated radionuclide production rates (e.g. [2]) should be used in place of the Geant4 physics models. Application of the existing cross section libraries to this study is premature, as other uncertainties such as GCR rate and SPE fluences and shapes at Psyche, as well as Psyche's surface composition, are currently unknown but will be better constrained prior to the beginning of low-altitude operations at Psyche.

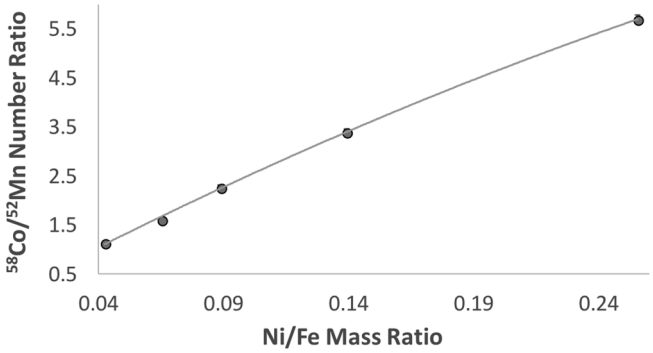

Fig. 6. Modeled ^{58}Co to ^{52}Mn number ratio, produced by a solar proton event (SPE) having a spectral shape identical to the solar proton environment detailed in Fig. 1A, as a function of the Ni-to-Fe mass ratio of the surface of Psyche. Model uncertainties are smaller than the data points. A second-order polynomial fit highlights the relationship between activation and surface composition.

7. Summary and conclusions

Measurements of induced radioactivity in samples irradiated with a 1 GeV proton beam were used to benchmark Geant4 models of cosmic-ray-induced activation of metal-rich surfaces in the solar system. The experiment identified gamma rays resulting from the decay of dozens of radioactive isotopes (Tables 1 and 2). Quantitative monitoring of gamma decays from the irradiated samples led to the characterization of ^{58}Co, ^{57}Co, ^{56}Co, ^{54}Mn, ^{52}Mn, ^{51}Cr, ^{48}V, ^{26}Sc, and ^{22}Na (Tables 3 and 4) production in the samples. The radionuclide production rates during irradiation were derived by fitting the decay rates and interpolating the activity to that at irradiation (Table 5). This information was used to benchmark a Geant4 model of cosmogenic radionuclide production (Table A3). We concluded that Geant4's Shielding physics list provided the best match to the measurements. That model reproduced the measured radionuclide production rates to within a factor of 2.5 for all of the elements listed above for both irradiated samples (Fig. 4), with perfect measurement-to-model agreement for all but two elements, within the statistical precision of the measurements.

The Geant4 model was subsequently extended to make predictions about cosmic-ray-induced activation of asteroid (16) Psyche, with the goal of identifying signatures that might be observable with the Psyche Gamma-Ray and Neutron Spectrometer (GRNS) during its low-altitude measurements of Psyche. Modeled production and decay rates were compared to background rates in the MESSENGER Gamma-Ray Spectrometer (GRS), acquired at a Psyche-equivalent orbit about Mercury (0.8 body radii). Note that the Psyche and MESSENGER gamma-ray sensors have identical sensor types and sizes, giving them similar gamma-ray detection efficiencies.

Our modeling indicates that galactic-cosmic-ray-induced radionuclide production and decay will not be observable from orbit by the Psyche GRNS. In contrast, solar-cosmic-ray-induced radionuclide decay, produced during a solar proton event (SPE) may be observable if the fluence of > 30 MeV protons is sufficiently high > 2×10^6 cm^{-2}. Such events have an inferred frequency at Psyche of ~1.6 yr^{-1}, making it plausible that such an event may occur during the planned 100-day-long GRNS low-altitude orbit at Psyche. If such an event

occurs, monitoring of the SPE-induced radionuclide decay curves following the SPE provides an independent means of characterizing the composition of Psyche's surface (e.g., Fig. 6), an important goal of the Psyche mission.

Acknowledgements

Our proton irradiation experiment and subsequent activation measurements was funded by NASAs Maturation of Instrumentation for Solar System Exploration (MatISSE) program, grant NNX15AF40G. Data interpretation and implications for the Psyche mission were funded by NASAs Discovery Program, Psyche: Journal to a Metal World mission, contract NNM16AA09C, under a subcontract from the Arizona State University to the Johns Hopkins Applied Physics Laboratory. We thank Adam Rusek, Michael Sivertz, Rory Rosselot, and Jimmy Williams of the NASA Space Radiation Laboratory (NSRL) at Brookhaven National Laboratory for assistance conducting the proton irradiation experiment. Finally, we thank an anonymous reviewer, whose thorough review prompted changes that improved this manuscript.

Appendix

A: Gamma-ray detection efficiency

A Geant4 model of the HPGe sensor, its housing, the samples, and the sample-to-detector geometry was used to estimate the gamma-ray detection efficiency of the measurements, and its uncertainty. Prior to simulating the efficiency for our sample measurements, we benchmarked the accuracy of our Geant4 detector geometry. First, we measured the efficiency for detecting 1332-keV gamma rays using a ^{60}Co source placed 25 cm from the front of the detector. This is an industry-standard means of measuring efficiency, and the result is typically quoted as the relative efficiency compared to that of a 3 cm × 3 cm NaI detector in the same geometry. We measured the relative efficiency of our HPGe detector to be 72.5%. The manufacturer-reported value is 73.5%. The Geant4-modeled value is 72.3%. This agreement confirmed the validity of our modeled efficiency in the standard geometry.

Our sample measurements were conducted in a non-standard geometry, with the samples placed 7.25 ± 0.50 cm beneath the detector, with the midpoint of the samples near the back end of the HPGe crystal. In this geometry, gamma rays must pass through more material than in the front-facing geometry. To benchmark our model in this geometry, we made measurements of a ^{54}Mn source in the center of the sample position. The measured efficiency (ε) times solid angle (Ω) for the 834-keV gamma rays from this source was 0.68%. The modeled $\varepsilon\Omega$ value was 0.78%, 15% higher than the measurements. We therefore adopted 15% as the uncertainty for all modeled $\varepsilon\Omega$ values in the sample measurement geometry.

To model $\varepsilon\Omega$ for the sample measurements, we simulated production of gamma rays (γ) with all energies of interest for this study. Gamma rays were randomly (homogenously) generated within the sample volume and emitted isotropically. The number of modeled events detected with their full energy in the HPGe was compared to the number of modeled histories, and the ratio of the two values provided $\varepsilon\Omega$ as a function of gamma-ray energy (E_γ). Note that $\varepsilon\Omega$ accounts for intrinsic gamma-ray detection efficiency, measurement solid angle, and gamma-ray attenuation losses within the sample. Note that here we define Ω to be the fraction field of the view of the sensor, as viewed by the sample, which is a unitless quantity.

Varying sample vertical placement, relative to the detector, over the known ± 0.25 cm precision for sample placement, yielded a 5% variation in $\varepsilon\Omega$ values over the entire energy range. Varying the horizontal position of the sample by 3 cm, the maximum variability in sample placement expected for the repeated measurements, results in 20% variations in $\varepsilon\Omega$. Adding the three known measurement uncertainties (5% from vertical position, 20% uncertainty from horizontal position, and 15% for Geant4 model accuracy) in quadrature yields a total uncertainty on $\varepsilon\Omega$ of 25%.

Appendix B

Geant4 modeling inputs

Tables A1 and A2 list the elemental compositions for the targets used in the proton irradiation experiment. Table A1 is the composition of the Campo del Cielo meteorite (Fig. A1), derived from analyses of other portions of the meteorite. Those analyses are detailed in Wasson and Kallemeyn [20]. Table A2 details the composition of our silicate target, a sample of Bronzite Pyroxenite (Fig. A1). The elemental composition of this material was derived from a PIXE-induced x-ray fluorescence investigation of multiple spots on a portion of the sample that was removed prior to preparing the sample subsequently used for the proton irradiation experiment. The uncertainty values listed correspond to the standard deviation of results

Table A1
Reference composition used for the Campo del Cielo meteorite.

Element	Concentration	
Fe	91.70	wt%
Ni	6.68	wt%
Co	0.46	wt%
S	0.40	wt%
C	0.37	wt%
P	0.28	wt%
Ge	394	ppm
Re	370	ppm
Cu	140	ppm
Ga	93	ppm
Cr	38	ppm
As	11.8	ppm
Pt	7.6	ppm
Ir	3.55	ppm
Au	1.29	ppm
W	0.31	ppm
Sb	0.27	ppm

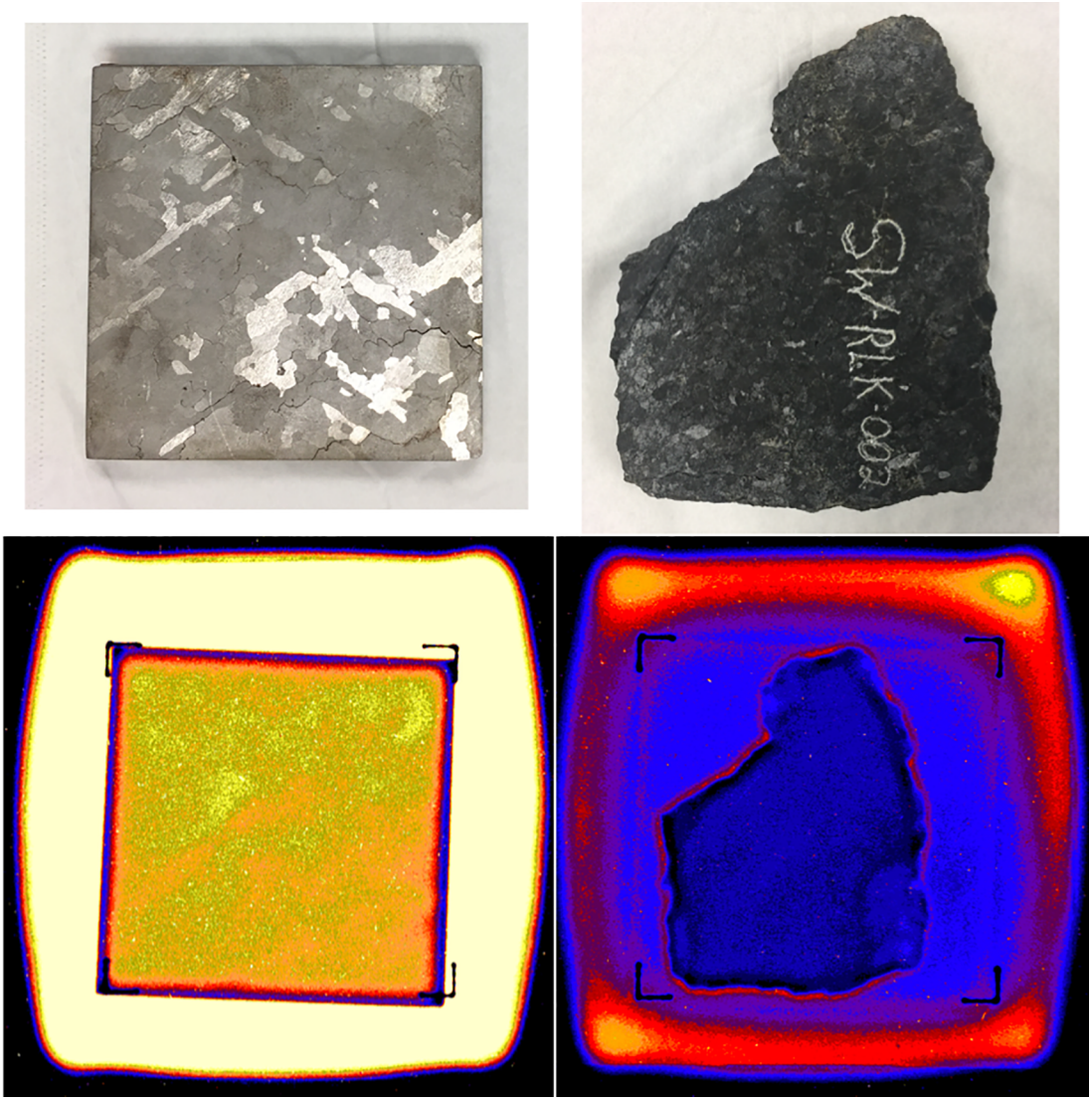

Fig. A1. Images (top panels) and proton radiographs (bottom panels), acquired with the NSRL downstream digital beam imager (Section 4.1), of the samples used for this study. Clockwise, from upper left: Campo del Cielo meteorite, Bronzite Pyroxenite (BP) silicate rock, proton radiograph of the BP target, proton radiograph of the Campo del Cielo target. For the radiographs, the color intensity scale, from low to high intensity, is blue-purple-red-orange-yellow-white. Intensity is not normalized. For the Campo del Cielo target, the relative orientation of the sample in the beamline may not be a match between the images. (For interpretation of the references to colour in this figure legend, the reader is referred to the web version of this article.)

from multiple spots on that sample. The values listed in both tables were used as inputs for the Geant4 model of the proton irradiation experiment. In principle, errors in these compositions may have contributed to element-by-element mismatches in the measured-to-modeled radionuclide production ratios (Fig. 4), however we have attributed those errors instead to the Geant4 physics model.

Geant4 modeling of the proton irradiation experiment was carried out using seven physics lists. For each physics list, 8×10^7 protons were incident on the target, and the number of nuclei produced for each isotope of interest during that irradiation was tallied. That number was divided by 8×10^7 to yield the number of nuclei produced per proton. That number was compared to the measured number of nuclei per proton (N_0/proton)

Table A2
Composition of the Bronzite Pyroxenite (BP) "silicate" sample, derived from a particle-induced x-ray emission analysis. Uncertainties are derived from spot analysis of different locations on the sample.

Element	Concentration (wt%)	Uncertainty (%)
Fe	8.41	6
Cr	0.10	7
Ca	1.88	6
Al	1.57	8
Si	22.49	3
Mg	18.67	9
O	48.52	10

Table A3
Results from the Geant4 physics list benchmarking activity, showing the measured-to-modeled radionuclide concentration ratio for each element measured during the long-term activation measurements.

		Energy (keV)	Measured N_0/proton[a]	Measured to modeled Ratio for each Geant4 physics list				
				QGSP_BIC_HP	QGSP_BERT_HP*	QGSP_INCLXX_HP*	Shielding$^{\Delta}$	QBBC
Iron Meteorite	^{58}Co	810	$(6.6 \pm 1.0) \times 10^{-4}$	1.3 ± 0.3	0.9 ± 0.2	1.0 ± 0.2	0.9 ± 0.1	2.4 ± 0.5
	^{57}Co	122	$(1.0 \pm 0.3) \times 10^{-3}$	1.2 ± 0.4	1.6 ± 0.6	1.1 ± 0.4	0.9 ± 0.3	1.1 ± 0.4
	^{56}Co	846	$(5.7 \pm 1.2) \times 10^{-4}$	0.05 ± 0.01	1.0 ± 0.3	0.4 ± 0.1	0.6 ± 0.1	0.4 ± 0.1
		1038	$(4.7 \pm 1.0) \times 10^{-4}$	0.04 ± 0.01	0.8 ± 0.2	0.4 ± 0.1	0.5 ± 0.1	0.4 ± 0.1
		1237	$(4.7 \pm 1.0) \times 10^{-4}$	0.04 ± 0.01	0.8 ± 0.2	0.4 ± 0.1	0.5 ± 0.1	0.4 ± 0.1
		1772	$(4.8 \pm 1.1) \times 10^{-4}$	0.04 ± 0.01	0.8 ± 0.2	0.4 ± 0.1	0.5 ± 0.1	0.4 ± 0.1
	^{54}Mn	835	$(6.2 \pm 2.3) \times 10^{-3}$	0.8 ± 0.3	1.3 ± 0.6	0.9 ± 0.4	1.3 ± 0.5	0.8 ± 0.3
	^{52}Mn	744	$(1.3 \pm 0.4) \times 10^{-3}$	0.5 ± 0.2	1.3 ± 0.4	0.6 ± 0.2	1.3 ± 0.4	0.5 ± 0.2
		936	$(1.2 \pm 0.4) \times 10^{-3}$	0.5 ± 0.2	1.2 ± 0.5	0.6 ± 0.2	1.2 ± 0.4	0.4 ± 0.2
		1433	$(1.3 \pm 0.4) \times 10^{-3}$	0.5 ± 0.2	1.2 ± 0.5	0.6 ± 0.2	1.2 ± 0.4	0.5 ± 0.2
	^{51}Cr	320	$(6.3 \pm 1.4) \times 10^{-3}$	1.1 ± 0.3	1.6 ± 0.4	1.4 ± 0.4	1.2 ± 0.3	1.1 ± 0.3
	^{48}V	944	$(2.0 \pm 0.3) \times 10^{-3}$	0.5 ± 0.1	2.5 ± 0.6	0.6 ± 0.1	0.9 ± 0.2	0.5 ± 0.1
		984	$(2.1 \pm 0.4) \times 10^{-3}$	0.6 ± 0.1	2.7 ± 0.7	0.7 ± 0.2	1.0 ± 0.2	0.5 ± 0.1
		1311	$(2.1 \pm 0.3) \times 10^{-3}$	0.6 ± 0.1	2.7 ± 0.6	0.7 ± 0.1	0.9 ± 0.1	0.5 ± 0.1
	^{46}Sc	889	$(1.0 \pm 0.3) \times 10^{-3}$	0.9 ± 0.3	2.4 ± 0.8	0.9 ± 0.3	2.4 ± 0.6	0.9 ± 0.3
		1121	$(9.4 \pm 2.4) \times 10^{-4}$	0.8 ± 0.3	2.3 ± 0.7	0.8 ± 0.3	2.2 ± 0.6	0.8 ± 0.3
	Mean ± Standard Deviation			0.6 ± 0.4	1.6 ± 0.7	0.7 ± 0.3	1.1 ± 0.6	0.7 ± 0.5
Bronzite Pyroxenite	^{54}Mn	835	$(1.8 \pm 1.1) \times 10^{-4}$	0.9 ± 0.6	1.6 ± 1.0	1.0 ± 0.7	1.6 ± 1.0	0.9 ± 0.6
	^{51}Cr	320	$(2.0 \pm 0.8) \times 10^{-4}$	1.2 ± 0.6	1.7 ± 0.8	1.6 ± 0.7	1.3 ± 0.5	1.2 ± 0.6
	^{48}V	984	$(8.4 \pm 2.3) \times 10^{-5}$	0.7 ± 0.2	3.5 ± 1.1	1.9 ± 0.6	1.2 ± 0.3	0.7 ± 0.2
	^{22}Na	1275	$(9.8 \pm 4.4) \times 10^{-4}$	0.6 ± 0.3	1.3 ± 0.7	0.6 ± 0.3	1.2 ± 0.5	0.6 ± 0.3
	Mean ± Standard Deviation			0.9 ± 0.3	0.9 ± 2.0	1.3 ± 0.6	1.3 ± 0.2	0.9 ± 0.3
Mean ± Standard Deviation (Both Samples)				0.64 ± 0.40	1.66 ± 0.77	0.82 ± 0.42	1.15 ± 0.50	0.75 ± 0.47

[a] Reproduced from Tables 3 and 4.
* FTFP_BERT_HP and FTFP_INCLXX_HP were also tested and the results were identical to the QGSP_BIC_HP and QGSP_BERT_HP values listed here.
$^{\Delta}$ Shielding and ShieldingLEND physics lists were both tested, and the results were identical.

measured in the target to yield the measured-to-modeled ratio. Table A3 lists these results for the QGSP_BIC_HP, QGSP_BERT_HP, QGSP_INCLXX_HP, Shielding, and QBBC physics lists. Note that FTFP_BERT_HP, FTFP_INCLXX_HP, and ShieldingLEND provided identical results to the respective lists (QGSP_BERT_HP, QGSP_INCLXX_HP, and Shielding), and thus those results were not reproduced in Table A3.

Appendix B. Supplementary data

Supplementary data to this article can be found online at https://doi.org/10.1016/j.nimb.2019.03.023.

References

[1] J. Masarik, R.C. Reedy, Effects of bulk composition on nuclide production processes in meteorites, Geochim. Cosmochim. Acta 58 (23) (1994) 5307–5317.
[2] R. Michel, I. Leya, L. Borges, Production of cosmogenic nuclides in meteoroids: accelerator experiments and model calculations to decipher the cosmic ray record in extraterrestrial matter, Nucl. Inst. Meth. Phys. Res. 113 (1996) 434.
[3] M. Honda, D. Lal, Spallation cross sections for long-lived radionuclides in iron and light nuclei, Nucl. Phys. 51 (1963) 363–368.
[4] R. Silberberg, C.H. Tsao, A.F. Barghouty, Updated partial cross sections of proton-nucleus reaction, Astrophys. J. 501 (1998) 911–919.
[5] M. Honda, J.R. Arnold, Effects of cosmic rays on meteorites, Science 143 (3603) (1964) 203–212.
[6] R.C. Reedy, A model for GCR-particle fluxes in stony meteorites and production rates of cosmogenic nuclides, J. Geophys. Res.: Solid Earth 90 (S02) (1985).
[7] I. Leya, H.J. Lange, S. Neumann, R. Wieler, R. Michel, The production of cosmogenic nuclides in stony meteoroids by galactic cosmic-ray particles, Meteorit. Planet. Sci. 35 (2) (2000) 259–286.
[8] S. Vogt, G.F. Herzog, R.C. Reedy, Cosmogenic nuclides in extraterrestrial materials, Rev. Geophys. 28 (3) (1990) 253–275.
[9] K. Nishiizumi, M.W. Caffee, J. Masarik, Cosmogenic radionuclides in Los Angeles martian meteorite, Meteorit. Planet. Sci. Supp. 35 (2000) A120.
[10] O. Eugster, Cosmic-ray exposure ages of meteorites and lunar rocks and their significance, Chemie der Erde-Geochemistry 63 (1) (2003) 3–30.
[11] L.T. Elkins-Tanton, E. Asphaug, J. Bell, D. Bercovici, B.G. Bills, R.P. Binzel, W.F. Bottke, J. Goldsten, R. Jaumann, I. Jun, D.J. Lawrence, S. Marchi, D. Oh, R. Park, P.N. Peplowski, C.A. Polansky, T.H. Prettyman, C.A. Raymond, C.T. Russell, B.P. Weiss, D.D. Wenkert, M. Wieczorek, M.T. Zuber, Asteroid (16) Psyche: the science of visiting a metal world, 47th Lunar and Planetary Science Conference, abstract, 2016, p. #1631..
[12] P.N. Peplowski, D.J. Lawrence, J.O. Goldsten, M. Burks, A.W. Beck, L.T. Elkins-Tanton, I. Jun, T.J. McCoy, T.H. Prettyman, Gamma-ray spectroscopy of asteroid 16 Psyche: expected performance of the Psyche Gamma-Ray, Spectrometer, 47th Lunar and Planetary Science Conference, abstract, 2016, p. #1394..
[13] O. Adriani, G.C. Barbarino, G.A. Bazilevskaya, R. Bellotti, M. Boezio, E.A. Bogomolov, L. Bonechi, et al., PAMELA measurements of cosmic-ray proton and helium spectra, Science 332 (6025) (2011) 69–72.
[14] G. Castagnoli, D. Lal, Solar modulation effects in terrestrial production of carbon-14, Radiocarbon 22 (2) (1980) 133–158.
[15] D. Lal, Theoretically expected variations in the terrestrial cosmic-ray production rates of isotopes, in: G.C. Castagnoli (Ed.), Solar-Terrestrial Relationships and the Earth Environment in the last Millenia, Proc. Int. Sch. Phys. Enrico Fermi, 1985, pp. 216–233.
[16] G.W. McKinney, D.J. Lawrence, T.H. Prettyman, R.C. Elphic, W.C. Feldman, J.J. Hagerty, MCNPX benchmark for cosmic ray interactions with the Moon, J. Geophys. Res. Planets 111 (E6) (2006).
[17] I.G. Usoskin, G.A. Bazilevskaya, G.A. Kovaltsov, Solar modulation parameter for cosmic rays since 1936 reconstructed from ground-based neutron monitors and ionization chambers, J. Geophys. Res.: Space Phys. 116 (A2) (2011).
[18] J. Feynman, A. Ruzmaikin, V. Berdichevsky, The JPL proton fluence model: an update, J. Atmos. Solar-Terrest. Phys. 64 (2002) 1679–1686.
[19] K. Ammon, J. Masarik, I. Leya, New model calculations for the production of cosmogenic nuclides in iron meteorites, Meteor. Planet. Sci. 44 (2009) 485–503.
[20] J.T. Wasson, G.W. Kallemeyn, The IAB iron-meteorite complex: a group, five subgroups, numerous grouplets, closely related, mainly formed by crystal segregation in rapidly cooling melts, Geochim. Cosmochim. Acta 66 (13) (2002) 2445–2473.
[21] R.G. Liberman, J.F. Niello, M.L. Di Tada, L.K. Fifield, J. Masarik, R.C. Reedy, Campo del Cielo iron meteorite: sample shielding and meteoroid's preatmospheric size, Meteorit. Planet. Sci. 37 (2) (2002) 295–300.
[22] J.A. Sanchez, V. Reddy, M.K. Shepard, C. Thomas, E.A. Cloutis, D. Takir, A. Conrad, C. Kiddell, D. Applin, Detection of rotational spectral variation on the M-type asteroid (16) Psyche, Astron. J. 153 (1) (2016) 29.
[23] D.I. Lowenstein, A. Rusek, Technical developments at the NASA Space Radiation

laboratory, Radiat. Environ. Biophys. 46 (2007) 91–94.
[24] N. Tsoupas, L. Ahrens, S. Bellavia, R. Bonati, K.A. Brown, I. Hung Chiang, C.J. Gardener, D. Gassner, S. Jao, W.W. Mackay, I. Marneris, W. Meng, D. Phillips, P. Pile, R. Prigl, A. Rusek, L. Syndstrup, K. Zeno, Uniform beam distributions at the target of the NASA Space Radiation Laboratory's beam line, Phys. Rev. ST Accel. Beams 10 (2007) 024701.
[25] C. La Tessa, M. Sivertz, I.-H. Chiang, D. Lowenstein, A. Rusek, Overview of the NASA space radiation laboratory, Life Sci. Space Res. 11 (2016) 18–23.
[26] S. Agostinelli, J. Allison, K. Amako, J. Apostolakis, H. Araju, P. Arce, M. Asai, D. Axen, S. Banerjee, G. Barrand, F. Behner, L. Bellagamba, J. Boudreau, L. Broglia, A. Brunengo, H. Burkhardt, S. Chauvie, J. Chuma, R. Chytracek, G. Cooperman, G. Cosmo, P. Degtyarenko, A. Dell'Acqua, G. Depaoloa, D. Dietrich, R. Enami, A. Feliciello, C. Ferguson, H. Fessefeldt, G. Folger, F. Foppiano, A. Forti, S. Garelli, S. Giani, R. Giannitrapani, D. Gibin, J.J. Gomez Cadenas, I. Gonzalez, G. Gracia Abril, G. Greeniaus, W. Greiner, V. Grichine, A. Grossheim, S. Guatelli, P. Grumlinger, R. Hamatsu, K. Hashimoto, H. Hasui, A. Heikkinen, A. Howard, V. Ivanchenko, A. Johnson, F.W. Jones, J. Kallenbach, N. Kanaya, M. Kawabata, Y. Kawabata, M. Kawaguti, S. Kelner, P. Kent, A. Kimura, T. Kodama, R. Kokoulin, M. Kossov, H. Kurashige, E. Lamanna, T. Lampen, V. Lara, V. Lefebure, F. Lei, M. Liendl, W. Lockman, F. Longo, S. Magni, M. Maire, E. Medernach, K. Minamimoto, P. Mora de Freitas, Y. Morita, K. Murakami, M. Nagamatu, R. Nartallo, P. Nieminen, T. Nishamura, K. Ohtsubo, M. Okamura, S. O'Neale, Y. Oohata, K. Paech, J. Perl, A. Pfeiffer, M.G. Pia, F. Ranjard, A. Rybin, S. Sadilov, E. Di, G. Salvo, T. Santin, N. Sasaki, Y. Savvas, S. Sawada, S. Scherer, V. Sei, D. Sirotenko, N. Smith, H. Starkov, J. Stoecker, M. Sulkimo, S. Takahata, E. Tanaka, E. Safai Tchemiaev, M. Tehrani, P. Tropeano, H. Truscott, L. Uno, P. Urban, M. Urban, A. Verderi, W. Walkden, H. Wander, J.P. Weber, T. Wellisch, D.C. Wenaus, D. Williams, T. Wright, H. Yamada, D. Zschiesche Yoshida, GEANT4 – a simulation toolkit, Nucl. Inst. Meth. A 506 (2003) 250–303.
[27] J. Allison, K. Amako, J. Apostolakis, H. Araujo, P. Arce Dubois, M. Asai, G. Barrand, R. Capra, S. Chauvie, R. Chytracek, G.A.P. Cirrone, G. Cooperman, G. Cosmo, G. Cuttone, G.G. Daquino, M. Donszelmann, M. Dressel, G. Folger, F. Foppiano, J. Generowicz, V. Grichine, S. Guatelli, P. Gumplinger, A. Heikkinen, I. Hrivnacova, A. Howard, S. Incerti, V. Ivanchenko, T. Johnson, F. Jones, T. Koi, R. Kokoulin, M. Kossov, H. Kurashige, V. Lara, S. Larsson, F. Lei, O. Link, F. Longo, M. Maire, A. Mantero, B. Mascialino, I. McLaren, P. Mendez Lorenzo, K. Minamimoto, K. Murakami, P. Nieminen, L. Pandola, S. Parlati, L. Peralta, J. Perl, A. Pfeiffer, M.G. Pia, A. Ribon, P. Rodrigues, G. Russo, S. Sadilov, G. Santin, T. Sasaki, D. Smith, N. Starkov, S. Tanaka, E. Tcherniaev, B. Tome, A. Trindade, P. Truscott, L. Urban, M. Verderi, A. Walkden, J.P. Wellisch, D.C. Williams, D. Wright, H. Yoshida, Geant4 developments and application, IEEE Trans. Nucl. Sci. 53 (1) (2006) 270–278.
[28] J. Allison, K. Amako, J. Apostolakis, P. Arce, M. Asai, T. Aso, E. Bagli, A. Bagulya, S. Banerjee, G. Barrand, B.R. Beck, A.G. Bogdanov, D. Brandt, J.M.C. Brown, H. Burkhardt, Ph. Canal, D. Cano-Ott, S. Chauvie, K. Cho, G.A.P. Cirrone, G. Cooperman, M.A. Cortes-Giralo, G. Cosmo, G. Cuttone, G. Depaola, L. Desorgher, X. Dong, A. Dotti, V.D. Elvira, G. Folger, Z. Francis, A. Galoyan, L. Garnier, M. Gayer, K.L. Genser, V.M. Grichine, S. Guatelli, P. Gueye, P. Gumplinger, A.S. Howard, I. Hnvnacova, S. Hwang, S. Incerti, A. Ivanchenko, V.N. Ivanchenko, F.W. Jones, S.Y. Jun, P. Kaitaniemi, N. Karkatsanis, M. Kelsey, A. Kimura, T. Koi, H. Kurashige, A. Lechner, S.B. Lee, M. Longo, D. Maire, A. Mancusi, E. Mantero, B. Mendoza, K. Morgan, T. Nikitina Murakami, P. Pandola, J. Paprocki, I. Perl, M.G. Petrovic, W. Pia, J.M. Pokorski, M. Quesada, M.A. Raine, A. Ribon Reis, A. Ristic Fira, F. Romano, G. Russo, G. Santin, T. Sasaki, D. Sawkey, J.I. Shin, I.I. Strakovsky, A. Taborda, S. Tanaka, E. Tcherniaev, B. Tome, T. Toshito, H.N. Tran, P.R. Truscott, L. Urban, V. Uzhinsky, J.M. Verbeke, M. Verderi, B.L. Wendt, H. Wenzel, D.H. Wright, D.M. Wright, T. Yamashia, J. Yarba, H. Yoshida, Recent developments in GEANT4, Nucl. Inst. Meth. A 835 (2016) 186–225.
[29] J.M. Quesada, V. Ivanchenko, A. Ivanchenko, M.A. Cortés-Giraldo, G. Folger, A. Howard, D. Wright, Recent developments in pre-equilibrium and de-excitation models in Geant4, Proc. Monte Carlo Conference (MC 10), (2010).
[30] Geant4 collaboration, (2015), Application Developers Guide: Version: geant4 10.2.
[31] K. Shibata, et al., JENDL-4.0: a new library for nuclear science and energineering, J. Nucl. Sci. Tech. 48 (2011) 1–30.
[32] Geant4 collaboration, (2015), Physics Reference Manual, Version: geant4 10.2.
[33] D.A. Brown, et al., ENDF/B-VIII.0: the 8th major release of the nuclear reaction data library with CIELO-project cross sections, new standards, and thermal scattering data, Nucl. Data Sheets 148 (2018) 1–142.
[34] J. Cugnon, A. Boudard, J.C. David, A. Kelić-Heil, S. Leray, D. Mancusi, M.V. Ricciardi, Production of heavy clusters (up to A = 10) by coalescence during the intranuclear cascade phase of spallation reactions, J. Phys.: Conf Series 312 (8) (2011) 082019.
[35] T.H. Prettyman, J.J. Hagerty, R.C. Elphic, W.C. Feldman, D.J. Lawrence, G.W. McKinney, D.T. Vaniman, Elemental composition of the lunar surface: analysis of gamma ray spectroscopy data from Lunar Prospector, J. Geophys. Res.: Planets 111 (E12) (2006).
[36] S. Karunatillake, J.M. Keller, S.W. Squyres, W.V. Boynton, J. Brückner, D.M. Janes, O. Gasnault, H.E. Newsom, Chemical compositions at Mars landing sites subject to Mars Odyssey Gamma Ray Spectrometer constraints, J. Geophys. Res.: Planets 112 (E8) (2007).
[37] L.G. Evans, et al., Major-element abundances on the surface of Mercury: results from the MESSENGER Gamma-Ray Spectrometer, J. Geophys. Res. 117 (2012) E00L07, https://doi.org/10.1029/2012JE004178.
[38] T.H. Prettyman, D.W. Mittlefehldt, N. Yamashita, D.J. Lawrence, A.W. Beck, W.C. Feldman, T.J. McCoy, H.Y. McSween, M.J. Toplis, T.N. Titus, P. Tricarico, Elemental mapping by Dawn reveals exogenic H in Vesta's regolith, Science 338 (6104) (2012) 242–246.
[39] P.N. Peplowski, D. Bazell, L.G. Evans, J.O. Goldsten, D.J. Lawrence, L.R. Nittler, Hydrogen and major element concentrations on 433 Eros: evidence for an L-or LL-chondrite-like surface composition, Meteorit. Planet. Sci. 50 (3) (2015) 353–367.
[40] D.J. Lawrence, W.C. Feldman, R.C. Elphic, J.J. Hagerty, S. Maurice, G.W. McKinney, T.H. Prettyman, Improved modeling of Lunar Prospector neutron spectrometer data: implications for hydrogen deposits at the lunar poles, J. Geophys. Res. Planets 111 (E8) (2006).
[41] D.J. Lawrence, W.C. Feldman, J.O. Goldsten, T.J. McCoy, D.T. Blewett, W.V. Boynton, L.G. Evans, L.R. Nittler, E.A. Rhodes, S.C. Solomon, Identification and measurement of neutron-absorbing elements on Mercury's surface, Icarus 209 (1) (2010) 195–209.
[42] K.E. Mesick, W.C. Feldman, D.D.S. Coupland, L.C. Stonehill, Benchmarking Geant4 for simulating galactic cosmic ray interactions within planetary bodies, Earth Space Sci. 5 (7) (2018) 324–338.
[43] M.K. Shepard, J. Richardson, P.A. Taylor, L.A. Rodriguez-Ford, A. Conrad, I. de Pater, M. Adamkovics, K. de Kleer, J.R. Males, K.M. Morzinski, L.M. Close, Radar observations and shape model of asteroid 16 Psyche, Icarus 281 (2017) 388–403.
[44] C.A. Polansky, D.M. Marsh, R.R. Moore, R.S. Park, M. de Soria-Santacruz Pich, D. Wenkert, L.T. Elkins-Tanton, D.A. Williams, R. Jaumann, D.J. Lawrence, C.T. Russell, Psyche Team, Psyche Science Operations Concept: Maximize Reuse to Minimize Risk, 2018 SpaceOps Conference, SpaceOps Conferences, AIAA 2018–2703 (2018), https://doi.org/10.2514/6.2018-2703.
[45] D.F. Lupishenko, I.N. Belskaya, F.A. Tupieva, Photometry of the M-Type Asteroid 21 Lutetia, Soviet Astron. Lett. 9 (1983) 358–360.
[46] A. Matter, M. Delbo, B. Carry, S. Ligori, Evidence of a metal-rich surface for the Asteroid (16) Psyche from interferometric observations in the thermal infrared, Icarus 226 (1) (2013) 419–427.
[47] P.S. Hardersen, M.J. Gaffey, P.A. Abell, Near-IR spectral evidence for the presence of iron-poor orthopyroxenes on the surfaces of six M-type asteroids, Icarus 175 (1) (2005) 141–158.
[48] S.E. Forbush, World-wide cosmic ray variations, 1937–1952, J. Geophys. Res. 59 (4) (1954) 525–542.
[49] E.N. Parker, Cosmic-ray modulation by solar wind, Phys. Rev. 110 (6) (1958) 1445.
[50] L.J. Gleeson, W.I. Axford, Solar modulation of galactic cosmic rays, Astrophys. J. 154 (1968) 1011.
[51] P.N. Peplowski, J.T. Wilson, A.W. Beck, M. Burks, J.O. Goldsten, D.J. Lawrence, Characterizing near-surface elemental layering on Mars using gamma-ray spectroscopy: a proof-of-principle experiment, Nucl. Inst. Meth. Phys. Res. B 415 (2018) 89–99.
[52] L.G. Evans, P.N. Peplowski, E.A. Rhodes, J.O. Goldsten, R.D. Starr, S.C. Solomon, The MESSENGER gamma-ray spectrometer: calibration and operations, Icarus 288 (2017) 186–200.
[53] I. Jun, R.T. Swimm, A. Ruzmaikin, J. Feynman, A.J. Tylka, W.F. Dietrich, Adv. Space Res. 40 (2007) 304–312.
[54] J. Feynman, S. Gabriel, Interplanetary Particle Environment, (1988) JPL Publ. 88-28, Pasadena, CA.
[55] D. Lario, M.-B. Kallenrode, R.B. Decker, E.C. Roelof, S.M. Krimigis, A. Aran, B. Sanahuja, Radial and longitudinal dependence of solar 4–13 MeV and 27–37 MeV proton peak intensities and fluences: Helios and IMP 8 observations, Astrophys. 653 (2006) 1531–1544.
[56] R. Michel, et al., Cross sections for the production of residual nuclides by low- and medium-energy protons from the target elements C, N, O, Mg, Al, Si, Ca, Ti, V, Mn, Fe Co, Ni, Cu, Sr, Y, Zr, Nb, Ha, and Au, Nucl. Inst. Meth. Phys. Res. B 129 (1997) 153–193.
[57] P.N. Peplowski, D.J. Lawrence, E.A. Rhodes, A.L. Sprague, T.J. McCoy, B.W. Denevi, L.G. Evans, J.W. Head, L.R. Nittler, S.C. Solomon, K.R. Stockstill-Cahill, Variations in the abundances of potassium and thorium on the surface of Mercury: results from the MESSENGER Gamma-Ray Spectrometer, J. Geophys. Res.: Planets 117 (E12) (2012).